

*Efficient modeling of wave generation and propagation in a
semi-enclosed estuary*

Authors

Sean C. Crosby¹² (sean.crosby@wwu.edu)

Cornelis M. Nederhoff³

Nathan VanArendonk¹²

Eric E. Grossman¹²

¹U. S. Geological Survey, 2885 Mission St., Santa Cruz, 95060, CA, USA¹²

²Western Washington University, 516 High St., Bellingham, 98225, WA, USA¹³

³Deltares USA, , 8601 Georgia Ave, Silver Spring,, 20910, MD, USA

This manuscript is a non-peer reviewed preprint that is currently under review for the Journal of Ocean Modelling by Elsevier

1 Highlights

2 **Efficient modeling of wave generation and propagation in a semi-enclosed estuary**

3 Sean C. Crosby, Cornelis M. Nederhoff, Nathan VanArendonk, Eric E. Grossman

- 4 • Computationally rapid approaches are similarly skilled to traditional SWAM implementation in a semi-enclosed
5 estuary
- 6 • A combination of look-up-table and linear transformation are skilled where waves are both remotely and locally
7 generated
- 8 • A coupled hydro-dynamic and SWAN simulations suggest strong wave-current interactions in the Strait of Juan
9 de Fuca

Efficient modeling of wave generation and propagation in a semi-enclosed estuary

Sean C. Crosby^{a,b,*}, Cornelis M. Nederhoff^{a,c}, Nathan VanArendonk^a and Eric E. Grossman^{a,b}

^aU. S. Geological Survey, 2885 Mission St., Santa Cruz, 95060, CA, USA

^bWestern Washington University, 516 High St., Bellingham, 98225, WA, USA

^cDeltares USA, , 8601 Georgia Ave, Silver Spring,, 20910, MD, USA

ARTICLE INFO

Keywords:

ocean waves

prediction

validation

reduced-computation

ABSTRACT

Accurate, and high-resolution wave statistics are critical for regional hazard mapping and planning. However, long-term simulations at high spatial resolution are often computationally prohibitive. Here, multiple rapid frameworks including fetch-limited, look-up-table (LUT), and linear propagation are combined and tested in a large estuary exposed to both remotely (swell) and locally generated waves. Predictions are compared with observations and a traditional SWAN implementation coupled to a regional hydrodynamic model. Fetch-limited and LUT approaches both perform well where local winds dominate with errors about 10-20% larger than traditional SWAN predictions. Combinations of these rapid approaches with linear propagation methods where remotely generated energy is present also perform well with errors 0-20% larger than traditional SWAN predictions. Model-model comparisons exhibit lower variance than comparisons to observations suggesting that, while model implementation impacts prediction skill, model boundary conditions (winds, offshore waves) may be a dominant source of error. Overall results suggest that with a relatively small loss in prediction accuracy, simulations computation cost can be significantly reduced (by 2-4 orders of magnitude) allowing for high resolution and long-term predictions to adequately define regional wave statistics.

1. Introduction

Accurate, long-term, and high-resolution wave predictions are needed to assess the flood risk at the coast where rising sea levels and changing coastal conditions may alter wave propagation, generation, and extreme conditions on the shoreline (Erikson et al., 2015; Sweet et al., 2022). Phase-averaged numerical models, *e.g.*, Simulating Waves Nearshore (SWAN, Booij et al., 1999), are the defacto approach to predicting wave generation and transformation at the coast. While rapidly implemented when boundary forcing is available, models like SWAN require large amount computation for high-resolution simulation over long time periods. To reduce the computational cost the standard SWAN implementation may be replaced by faster reduced physics model (*e.g.*, O'Reilly and Guza, 1993; Leijnse et al., 2021) or by utilizing a look-up-table (LUT) approach (*e.g.*, Hegermiller et al., 2017). By neglecting the physics of sources, sinks, and non-linear interactions, wave energy is rapidly transformation is rapidly computed (Longuet-Higgins, 1957; Dorrestein, 1960; Crosby et al., 2018). This reduced physics approach is skillful where neglected terms are small, such as locations like the U. S. West Coast where low-frequency energy dominates. Here, the Coastal Data Information Program (CDIP, <https://cdip.ucsd.edu/>) makes operational wave predictions from buoy observations and linearly propagating wave energy to the shore (O'Reilly and Guza, 1993; O'Reilly et al., 2016).

*Corresponding author

sean.crosby@wwu.edu (S.C. Crosby); (C.M. Nederhoff); (N. VanArendonk); (E.E. Grossman)
Crosby, Nederhoff, VanArendonk, Grossman, et al. Preprint submitted to Elsevier
(S.C. Crosby); (C.M. Nederhoff); (N. VanArendonk); (E.E. Grossman)

ORCID(S):

49 Prior work has also shown that along the shelf of Oregon and Washington, wind-wave generation is small compared
50 to remotely-generated swell (García-Medina et al., 2013), illustrating why these rapid transformation approaches are
51 so successful.

52 In contrast, a look-up-table (LUT) is typically a suite of simulations for a variety of forcing combinations with
53 the complete model physics. The computation reduction comes from discretizing the range of possible forcings. This
54 finite set of simulations is computed once and then predictions are simply queried for a given forcing condition. For
55 example, in a small enclosed basin where wind conditions are spatially homogeneous, wind speeds and directions
56 can be binned into discrete values covering the expected range and used as the set of plausible forcings. Waves
57 are modeled for finite combination of speeds and directions forming a look-up table from which to generate rapid
58 predictions (Golshani, 2011; Elliott and Neill, 2015). Similar approaches have been applied to the transformation of
59 offshore waves to the nearshore (Hegermiller et al., 2017), but difficulties arise when the range of forcing conditions
60 can not be characterized within a manageable dimension, and total number of required simulations. For example,
61 if local wind conditions and offshore waves are relatively uncorrelated the number of dissimilar forcing conditions,
62 *i.e.*, offshore wave height, period, direction, wind speed, wind direction, becomes large. Additionally, offshore waves
63 may not be well represented by a single set of bulk wave parameters (Kumar et al., 2017) or require additional spectral
64 details (Crosby et al., 2016). Increasingly sophisticated statistical-modeling approaches have been developed to classify
65 weather patterns, and using clustering and dissimilarity algorithms to generate a suite of possible model forcing (Camus
66 et al., 2011, 2013); however, such approaches may fail with novel forcing conditions.

67 Reduced physics and LUT approaches both provide a trade-off between accuracy and the required computation
68 and may be more appropriate in specific regions or frequencies. Here, we quantify the trade-off between accuracy and
69 computational cost for several model implementations in a semi-enclosed estuary where both remotely and locally
70 generated waves are significant. Section 2 introduces the region and prior wave studies are reviewed. Observations
71 sites and data are reviewed in Section 3.1 and the varying modeling approaches are described in Section 3. Model skill
72 and comparison throughout the region are assessed in Section 4, including the impacts of currents on waves in the
73 region. Lastly, conclusions and results are summarized in Section 5

74 **2. Regional Background**

75 The Salish Sea is a semi-protected estuary on the Washington and British Columbia coast. Glacially carved, it
76 is a system of narrow straits, islands, sills, and basins all at varying spatial scales (Fig. 1). Exposed partially to the
77 NE Pacific Ocean, both locally- and remotely generated waves are observed, with their relative impact depending on
78 exposure. Strong currents (up to 5 m/s) in narrow tidal channels occur due to a large tidal range (3-4 m) and tidal prism
79 (Thompson and Thomson, 1994).

80 Waves in the Salish Sea contribute to flooding at high water levels; erode unconsolidated shorelines, bluffs, and
81 marshes; drive nearshore transport of sediments and pollutants important to shellfish, forage fish, and salmon habitats;
82 and affect recreational and commercial boating activities that provide critical access to the many islands in the Puget
83 Sound. Accurate, high-resolution, long-term wave predictions are thus critical to support shoreline planning, ecosystem
84 restoration, and regional navigation and transportation (Finlayson, 2006b; Yang et al., 2019; Battalio et al., 2005; W. J.
85 et al., 1997)

86 Prior wave modeling studies, despite the region's complexities, show good predictive skill. Early predictions
87 at Cama beach, located on Camano Island (Fig. 1), showed wave conditions are well modeled under stationary
88 assumptions, likely because in the enclosed region with relatively short fetches local wind-wave generation reaches
89 saturation rapidly (Finlayson, 2006a). A more recent regional wave study shows good skill at three moored buoy
90 locations in the Strait of Juan de Fuca (SJF) and Strait of Georgia (SoG) with an unstructured grid and non-stationary
91 model physics (Yang et al., 2019). The authors note the need to downscale wind predictions from 32 to 12km to
92 capture wind speeds in the region and derive a regional climatology based on a computationally costly, 5-year model
93 simulation.

94 Though initial studies show predictive skill, comparison were made at the few wave observation sites and
95 uncertainties remain regarding the impact of water levels and currents. Early observations suggest strong modulation
96 of wave heights by tidal currents in the SJF, (Lambrakos, 1981), but model studies are still lacking. Recent work has
97 shown significant impacts to waves by currents globally (Ardhuin et al., 2017; Gallet and Young, 2014) and in the Gulf
98 Stream (Hegermiller et al., 2019); given the magnitude of currents in the region significant wave impacts are probable.
99 To date, model validation of nearshore waves and their transformation and impacts across the shoreface are limited to
100 the Cama Beach study (Finlayson, 2006a), despite recent flood impacts associated with waves. Rapid, accurate, and
101 high-resolution approaches are needed to support ongoing flood hazard risk assessment.

102 **3. Methods**

103 Several wave modeling approaches were implemented, ranging in complexity from simple parameterized fetch-
104 and depth-limited predictions, to numerical coupled hydrodynamic and wave simulations and are detailed below. In
105 most cases waves were simulated from March 2016 - December 2020 where high resolution meteorological forcing
106 (Section 3.2.1) and observations (Section 3.1) are available.

107 **3.1. Observations**

108 Historic wave observations in the Salish Sea are sparse. The National Data Buoy Center (NDBC) currently
109 maintains directional 3-m disc buoys located at the estuary entrance (46087) and inside the SJF (46257, 46088).

Table 1

Locations and occupations of wave observations including short-term U. S. Geological Survey (USGS) bottom-mounted pressure sensor deployments and long-term National Data Buoy Center (NDBC) and Environment Canada (EC) directional wave buoy stations.

ID	Name	Lat[°]	Lon[°]	Depth [m]	Occupation
<i>NDBC buoys</i>					
46087	Neah Bay	48.493	-124.726	260	2004-Present
46088	Hein Bank	48.334	-123.165	114	2004-Present
46257	Angeles Point	48.173	-123.607	114	2020-Present
<i>Environment Canada buoys</i>					
46146	Halibut Bank	49.240	-123.730	42	1992-Present
46131	Sentry Shoal	49.910	-124.990	14	1992-Present
<i>U. S. Geological Survey</i>					
Spot-01	Bellingham Bay	48.742	-122.549	20	2/9/2020 - 1/2/2021
W1	Joseph Whidbey	48.318	-122.712	3	4/22/2019 - 9/4/2019
W2	Hastie Lake	48.274	-122.742	2	4/22/2019 - 9/4/2019
W3	Fort Ebey	48.227	-122.772	2	4/22/2019 - 9/4/2019
B1	Nooksack Delta	48.757	-122.551	4	12/11/2017 - 1/24/2018
B2	Squalicum	48.761	-122.519	3	12/11/2017 - 1/24/2018
B3	Post Point	48.715	-122.520	4	12/11/2017 - 1/24/2018
S1	Skagit Delta	48.335	-122.522	4	12/11/2017 - 2/9/2018
S2	Martha's	48.372	-122.551	3	12/11/2017 - 2/9/2018
S3	SneeOosh	48.396	-122.543	4	12/11/2017 - 2/9/2018

110 Environment Canada additionally maintains two directional buoys in the SoG (46146 and 46131), see Figure 1. To
 111 provide additional validation observations, including those close to shore, shallow bottom-mounted pressure gauges
 112 were deployed in Bellingham Bay (Fig. 1b), Skagit Bay, and on the west shore of Whidbey Island (Fig. 1c) for several
 113 months (Crosby and Grossman, 2019). Sites spanned a range of environments, from large to small basins, and with
 114 varying exposure to locally and remotely generated waves (Fig. 1). Wave conditions from pressure sensor observations
 115 were estimated following Jones and Monismith (2007).

116 3.2. Model Inputs -test

117 3.2.1. Meteorological Forcing

118 Winds and pressure fields were extracted from archived weather forecasts by Environment Canada (<https://weather.gc.ca/>), the highest resolution weather products freely available in the region. This High Resolution
 119 Deterministic Prediction System (HRDPS) is available at 1-hour temporal and at 2.5km spatial resolution with forty-
 120 eight hour forecasts every 6-hours. Surface winds (10-m) are from the HRPDS-West domain were extract from forecast
 121 hours 1-6 and concatenated together to create a continuous time series of wind forcing. The zero forecast hour, or
 122 analysis, was found to be inconsistent with observations and therefore not used. Archived forecasts from March 2016
 123 through 2020 provide nearly 5-years of forcing.
 124

125 3.2.2. Bathymetry

126 Model depths were derived from high resolution bathymetry available in the region including 1-m digital elevation
 127 models (DEMs) by the U. S. Geological Survey (Tyler et al., 2020, 2021), 10-m coastal DEM by the National
 128 Ocean and Atmospheric Administration (NOAA, SJF & Port Townsend, Washington 1/3-arc second datasets, <https://www.ncei.noaa.gov/>),
 129 3-arc second bathymetry dataset of British Columbia (<https://www.ncei.noaa.gov/>)
 130 and GEBCO 15-arc second global ocean and terrain model ([https://www.gebco.net/data_and_products/
 131 gridded_bathymetry_data/](https://www.gebco.net/data_and_products/gridded_bathymetry_data/)). Bathymetry sources were merged with priority given to higher resolution and more
 132 recent sources, and then spatially averaged at model resolution before interpolation to model grids.

133 3.2.3. Offshore waves

134 The frequency-directional wave spectrum at the wave model offshore boundary is estimated from directional wave
 135 buoy observations at 46087 (Fig. 1). The NDBC buoy is located at the entrance to the SJF. Although directional
 136 spread estimates by the NDBC 3-m discus observations have been found to contain bias (approximately 6-deg), mean
 137 direction observations are skillful (O'Reilly et al., 1996), and energy propagation into the SJF is likely modulated at
 138 1st order by offshore wave direction. The distribution of wave energy across offshore directions are estimated with
 139 observed directional moments (a_1, b_1, a_2, b_2 , Longuet-Higgins et al., 1963) and the maximum entropy method (MEM,
 140 Lygre and Krogstad, 1986). While the directional distribution estimated from directional wave bouy observations is
 141 inherently uncertain (Ochoa and Delgado-González, 1990), model predictions driven by the MEM have previously
 142 been observed to be skillful (O'Reilly et al., 2016; Crosby et al., 2016).

143 3.3. Models

144 3.3.1. Hydrodynamic model

145 A depth-averaged hydrodynamic model was developed for the Salish Sea by (Tehranirad et al., 2023) and
 146 summarized here. The Delft3D Flexible Mesh hydrodynamic model (Delft3D FM, Kernkamp et al., 2011) was
 147 developed with a spatial resolution varying from 150 to 1000-m. Surface and pressure forcing was derived from
 148 HRPDS forecasts. Offshore water levels were prescribed with tidal harmonics (Lyard et al., 2017, , FES2014b) and non-
 149 tidal water levels derived from HYbrid Coordinate Ocean Model (HYCOM, <https://www.hycom.org/>). Because
 150 HYCOM predictions do not include the inverse-barometer-effect, a reference pressure of 1017mb is used in the model
 151 to capture changing water levels owing to atmospheric pressure adjustments. Fluvial forcing is prescribed for 23 major
 152 rivers in the region with USGS gauge data (Survey, 2016) and Canadian observations of the Fraser River at Hope,
 153 British Columbia (station 08MF005) (Canada, 2019). Modeled water level predictions have average errors of 15cm.

Table 2

Model domain (Fig. 1), the domain which it is nested, and its spatial resolution.

Model	Domain	Nest In	Resolution [m]
LSR	LSR	-	100
LUT	L1	-	100
	L2	L1	50
NWM/SWM	D1	-	1000
	D2	D1	200
	D3	D1	200
	D4	D1	200
	D5	D4	50
	D6	D3	50

154 3.3.2. Linear-Shoaling-Refraction (LSR)

155 Shoaling and refraction processes dominate wave propagation when wind-wave generation and non-linear processes
 156 are small (O'Reilly and Guza, 1993). This is often the case on the U.S. West coast when long-period remotely generated
 157 wave energy propagates in deep water over the relatively short continental shelf. Several prior studies have shown that
 158 good predictive skill is achieved with simple shoaling and refraction transformation of wave energy (O'Reilly and
 159 Guza, 1991, 1993; Crosby et al., 2016), and these techniques are currently used operationally by the CDIP to make
 160 accurate nearshore wave predictions (O'Reilly et al., 2016).

161 By ignoring wind-wave generation and non-linear interactions, nearshore and offshore wave energy can be
 162 related through a simple linear transformation. Historically this transformation was estimated by backward ray-tracing
 163 (Longuet-Higgins, 1957; Dorrestein, 1960; Mehaute et al., 1982). More recently transformations derived from phase-
 164 averaged wave modeling were shown to be similar when spatial resolution was sufficient (Crosby et al., 2018). Here, the
 165 phase averaged wave model, Simulating WAVes Nearshore (SWAN, Booij et al., 1999), is used to relate offshore and
 166 nearshore wave energy in the SJF (Fig. 1) by simulating incoming wave energy from the range of possible directions.

167 The SWAN model domain covers the portion of the Salish Sea exposed to remote wave energy propagation through
 168 the SJF (Fig. 1, blue box). The model is run with varying incident wave direction, from 180 to 360-degrees at a 2-deg
 169 increments, covering the range of possible incident directions (*e.g.*, Fig. 2). Incoming wave energy, equivalent to 1-m
 170 in wave height, is prescribed at the boundary in a narrow 2-degree direction bin uniformly distributed across frequency
 171 for each simulation, similar to the approach in Crosby et al. (2018). The model is run in stationary mode (ignoring
 172 estimated propagation time-lags of 3-4 hours) with 180 direction bins (2-deg resolution) and 48 frequency bins spaced
 173 logarithmically from 0.04 Hz to 0.5Hz and at a spatial resolution of 100-m (Table 2). Simulations were run with constant
 174 water level equal to mean-sea-level (MSL) and currents were ignored. Second order numerics (SORDUP) produced
 175 significant garden sprinkler effect (see SWAN technical manual) and therefore first order (BSBT) propagation numerics
 176 were used. Wind-wave generation, white-capping, and diffraction are all disabled while bottom friction and breaking

Table 3

Model description and prescription of model forcing with a yes/no (Y/N) flag indicating if the model was forced by offshore waves (Offshore), regional winds (Wind), regional currents (Currents) and a flag to indicate whether stationary (S) or non-stationary (N) numerics were used in SWAN simulations. Simulated time periods are denoted with an X.

Model	Description	Offshore	Wind	Currents	Numerics	2016-2020	Oct-Nov 2019
FDL	fetch-depth-limited	N	Y	N	-	X	
LSR	linear-shoaling-refraction	Y	N	N	S	X	
LUT	SWAN look-up-table	N	Y	N	S	X	
SWM	stationary SWAN	Y	Y	N	S		X
SWM+C	stationary SWAN + current	Y	Y	Y	S	X	
NWM+C	non-stationary SWAN + current	Y	Y	Y	N		X

177 constants are set to default values. Convergence criteria was met for all simulations, requiring that in over 99% of cells
 178 the change in wave heights change were less than 2% or 2cm between the last and prior iteration. Computation of all
 179 model simulations on a 12-core desktop (AMD Ryzen 3.8GHz) at 100-m resolution took less than 1-day. Throughout
 180 this study SWAN version 41.10 or later (41.20 and 41.31) were used.

Frequency-directional energy spectra are saved at observation sites and at model grid cells (Fig. 1). Following Crosby et al. (2018), transform coefficients, K , are estimated from the ratio of nearshore, E_n , and offshore energy, E_o such that at location i ,

$$K[i, f, \theta_o, g(\theta_n)] = \frac{\int E_n(i, f, \theta_n) g(\theta_n) d\theta_n}{E_o(f, \theta_o)}, \quad \text{where } g(\theta_n) = (1, \cos \theta_n, \sin \theta_n, \cos 2\theta_n, \sin 2\theta_n). \quad (1)$$

The function $g(\theta_n)$ allows for an estimate of total wave energy and directional buoy moments $a1, b1, a2, b2$, respectively Longuet-Higgins et al. (1963). Offshore frequency-directional spectra at the model boundary, E_b , are estimated from observations at 46087 (Section 3.2.3). A simple integration of the offshore spectra and transform coefficients provides predictions of wave energy, E , at a time step, t , where

$$E(t, f) = \int K(f, \theta_o, 1) E_b(t, f, \theta_o) d\theta_o, \quad (2)$$

and predictions of directional moments, *e.g.*, a_1 , are similarly estimated,

$$a_1(t, f) = \int K(f, \theta_o, \cos \theta_n) E_b(t, f, \theta_o) d\theta_o. \quad (3)$$

181 Predictions are made within the model domain (LSR, Table 3) for the period of available HRDPS meteorological
 182 forecasts (Section 3.2.1).

183 **3.3.3. Fetch-depth-limited (FDL)**

While LSR models wave propagation, other methods are needed for for wind-wave generation. Over decades empirical relations between wind, waves, fetch, and water depth been developed and is best described by the non-dimensional variables: non-dimensional energy, $\epsilon = g^2 E/u^4$, non-dimensional frequency, $\nu = f_p u/g$, non-dimensional fetch, $\chi = gx/u^2$, and non-dimensional depth, $\delta = gd/u^2$. Here, g is the gravitational constant, E is the wave energy variance in m^2 , u is the wind speed, f_p is the peak wave period, and x is fetch. The comprehensive JONSWAP experiment in the North Sea (Hasselmann et al., 1973) was the first to use multiple observations sites with varying fetches and derived empirical relationships for ϵ and ν are found in CERC (1984). Lacking similar data in shallow water, Young and Verhagen (1996) examined an array of shallow wave observations in Lake George, Australia. An array of observations sites in the shallow lake (nearly constant 2-m depth) provided additional constraints and relationships for ϵ and ν where

$$\begin{aligned} \epsilon &= 3.64 \cdot 10^{-3} \left[\tanh A_1 \tanh \left(\frac{B_1}{\tanh A_1} \right) \right]^{1.74}, \\ \nu &= 0.133 \left[\tanh A_2 \tanh \left(\frac{B_2}{\tanh A_2} \right) \right]^{-0.37}, \end{aligned} \quad (4)$$

and

$$\begin{aligned} A_1 &= 0.493 \delta^{0.75}, \\ B_1 &= 3.13 \cdot 10^{-3} \chi^{0.57}, \\ A_2 &= 0.331 \delta^{1.01}, \\ B_2 &= 5.215 \cdot 10^{-4} \chi^{0.73}. \end{aligned} \quad (5)$$

These relations are used to estimate significant wave height, H_s , and peak period, T_p where

$$H_s = 4 \sqrt{u^4 \epsilon / g^2}, \quad T_p = \frac{u}{\nu g}. \quad (6)$$

Fetch, x , is estimated by tracing rays from a given location until they reach land, defined as a water depth less than 1-m (e.g., 3). Rays are traced in spherical coordinates by integrating the geodesic equations at 100-m steps (Munk et al., 1988) where a 100-m step size was found to be sufficient to avoid missing small islands and narrow spits. Rays are traced from the prediction site at a starting angle, θ , from 0-360 degrees with 1-deg increments. Tracing yields a

function $x(\theta)$ (e.g., Fig 3a). For a given wind direction, θ_w , the effective fetch, \hat{x} is

$$\hat{x} = \frac{\int x^\alpha(\theta)W(\theta, \beta) d\theta}{\int x^{\alpha-1}(\theta)W(\theta, \beta) d\theta} \quad (7)$$

where

$$W(\theta, \beta) = \begin{cases} \cos^{2\beta}(\theta - \theta_w) & \text{where } -\pi/2 \geq \theta \leq \pi/2 \\ 0 & \text{otherwise} \end{cases} \quad (8)$$

184 Here, $W(\theta, \beta)$ is a weighting function with width determined by β . Scaling parameter α determines the emphasis of
 185 peaks in $F(\theta)$, where a large alpha weights peaks more heavily than valleys. Small values of β result in a wide weighting
 186 function that considers a larger range of fetch values surrounding a given wind direction (e.g., A1). The largest \hat{x} are
 187 therefore derived from large α and small β values by allowing for a broad weighting function and weight peaks heavily
 188 (Fig. 3b). The weighting in (7) results in a smoother change in fetch with direction and tends to ignore small islands
 189 that wave energy is likely to refract or diffract around (O'Reilly and Guza, 1993). Additionally, α and β allow for tuning
 190 based on observations. Optimal values of $\beta = 1$ and $\alpha = 1$ were selected based on overall agreement with observations
 191 (see Appendix, section A.2)

192 Wind direction, θ_w , and speed, u , from HRDPS forecasts are extracted at the prediction location. The argument
 193 may be made for extracting wind speed from some upwind direction, but for simplicity only wind conditions at the
 194 prediction location are used. Water depths at each modeled time-step, d , are derived from numerical hydrodynamic
 195 simulations described in Section 3.3.1.

196 3.3.4. Look-up-table (LUT)

197 An alternative to the simple and computationally fast FDL approach, is the incrementally more sophisticated and
 198 computationally taxing method of creating a look-up-table (LUT) of pre-computed wave simulations. A LUT is an
 199 approach to reducing computation when forcing conditions can be parameterized into a small number of variables, and
 200 those forcing combinations can be pre-computed over the range of expected values. When the number of combinations
 201 is less than the time-steps of the simulation computation costs are reduced. Prior wave studies have applied a LUT
 202 approach to transform waves nearshore (Hegermiller et al., 2017) and predict wind-wave generation in enclosed basins
 203 (Elliott and Neill, 2015; Golshani, 2011). For wind-wave generation, wind conditions are assumed homogeneous across
 204 the model domain and a range of wind speeds and directions are simulated.

205 Here, stationary SWAN simulations are computed for a suite of wind speeds, 0 to 30 m/s in 2.5 m/s increments,
 206 wind directions, 0 to 360° in 20° increments, and water levels, -2 to 8.5 m+navd88 in 1.5 m increments for a total of

207 1,728 model runs (e.g., Fig. 4). Two model domains cover the region, L1 and L2, with directional resolution of 100m
 208 and 50m, respectively (Tables 2 and 3). Domain L2 is nested inside of domain L1 along the north-west boundary (Fig.
 209 1). The models are run in stationary mode with 72 direction bins (5-deg resolution) and 45 frequency bins spaced
 210 logarithmically from 0.03 Hz to 2.0Hz with default third generation wave growth and white-capping parameters.
 211 Diffraction is disabled and bottom friction and breaking constants are set to default values. Convergence criteria were
 212 set similarly to LSR simulations (Section 3.3.2). Computation is performed on the USGS computer cluster, Yeti (USGS
 213 Advanced Research Computing, 2021), requiring 36-days of compute on a single 20-core node (Intel Ivy Bridge).
 214 Several nodes were used simultaneously allowing for computation to complete in several days.

215 Wave predictions are generated at given locations with local water level predictions (Section 3.3.1) and the nearest
 216 over-water wind predictions (Section 3.2.1). At each time-step the LUT of desired wave parameters (e.g., H_s , T_p ,
 217 T_m , D_m) is linearly interpolated (3-dimension) to the predicted water level, wind speed, and wind direction. Predicted
 218 energy spectra, $E(f)$, is similarly interpolated at observation locations where spectral predictions are saved. Predictions
 219 are created over the time period with available HRDPS forecasts (2016-2020).

220 3.3.5. *LSR+FDL and LSR+LUT*

Combining the LSR predictions with FDL or LUT predictions offers a computationally rapid approach to capturing
 both offshore energy penetration and regional wind-wave generation. These calculations are done under the following
 assumptions: 1.) wind-wave generation is unaffected by existing sea state; 2.) nonlinear wave-wave interactions between
 locally generated and remotely generated waves are insignificant; and 3.) that all simplifying assumptions in LSR and
 LUT are additionally valid. Under these assumptions wave energy spectra from remote- and local-generation is simply
 additive. In practice, file storage limitations do not allow for saving frequency-directional spectra at all time steps and
 model locations. However, where only bulk parameter predictions are saved wave heights can be added in quadrature
 (e.g., $H_s^{(3)2} = H_s^{(1)2} + H_s^{(2)2}$), and mean frequency, f_m , is determined by a weighted average,

$$f_m^{(3)} = \frac{H_s^{(1)2} f_m^{(1)} + H_s^{(2)2} f_m^{(2)}}{H_s^{(1)2} + H_s^{(2)2}}. \quad (9)$$

221 Mean wave directions can be similarly estimated by a weighted average, but with care taken to use a circular mean;
 222 however this was not done here.

223 3.3.6. *Stationary and non-stationary wave model (SWN, SWM+C, NWM)*

224 A more robust, but computationally demanding approach to wave prediction, is implementation of a phase averaged
 225 wave model for continuous simulation. Here, SWAN was coupled to the regional hydrodynamic model of water
 226 level and currents (Section 3.3.1) with the Delft3D Flexible Mesh Modeling Suite developed by Deltares. SWAN

227 was configured in both stationary and non-stationary modes as well as with and without coupling to depth-averaged
228 currents. Spatially varying winds from HRDPS (Section 3.2.1) provide input to local wind-wave generation and waves
229 observed at 46087 (Section 3.2.3) provide offshore (spectral) forcing.

230 To allow for feasible computation a large overall SWAN domain was created at 1km spatial resolution with several
231 nested, and sub-nested domains (Table 2, Fig. 1) at resolutions increasing with a factor 5 to 200-m (nested) and 50-m
232 (sub-nested). Nested domains are created at locations with available observations and much of the larger region was
233 not resolved beyond the relatively coarse 1-km.

234 To evaluate differences and model skill three configurations were simulated, stationary numerics without wave-
235 current interactions (SWM), stationary numerics with wave-current interactions (SWM+C), and non-stationary
236 numerics with wave-current interactions (NWM+C). A time step of 10-min was used in non-stationary simulations,
237 while outputs and stationary simulations were computed at hourly intervals. The models are similar to LUT simulations
238 (Section 3.3.4, however the number of direction bins was reduced to 36 (10-deg resolution) to lower computational
239 expense. Convergence criteria were set similarly to LSR simulations (Section 3.3.2) but with a maximum number of
240 iteration of 50 in the stationary simulations. It was found to be necessary in non-stationary simulations to increase the
241 maximum number of iterations from the default of 1 to 10.

242 3.4. Simulation time periods

243 Wave simulations were performed over two time periods (Table 3). Owing to computational constraints, SWM,
244 SWM+C, and NWN+C simulations were completed during the comparatively short 2-month period from October
245 to November of 2019. Longer 5-year simulation were computed for SWM+C and all rapid approaches (FDL, LSR,
246 LUT) from 2016-2020 where both HRDPS wind forcing (Section 3.2.1) and regional wave observations were available
247 (Table 1).

248 4. Results and Discussion

249 Overall results suggest that including additional physics in numerical models tends to improve prediction skill,
250 however, this improvement is in some cases marginal and may not be worth the computational expense. Below,
251 predictions with stationary and non-stationary numerics are compared, the impact of wave current interactions are
252 evaluated, and reduced-physics model implementations are compared.

253 4.1. Non-stationary vs stationary

254 Stationary and non-stationary simulations should begin to diverge where the domain is large enough such that
255 the sea state does not fully develop within the model time step (1-hour). Comparisons of SWM+C and NWM+C
256 significant wave height (H_s) predictions from Oct-Nov 2019 show the largest root-mean-squared-differences (RMSD)

Table 4

Root-mean-square-error (RMSE) and bias at three observation sites (rows) for three model configurations (rows) for the simulation period Oct-Nov 2019 (Table 3).

Site	<i>Hs</i> RMSE [cm]			<i>Hs</i> bias [cm]		
	SWM	SWM+C	NWM+C	SWM	SWM+C	NWM+C
46257	30	31	29	6.0	6.6	7.6
46146	23	-	18	-3.0	-	-2.1
Spot-01	13	13	12	1.1	1.0	1.2

of 5-10 cm in the regions with the largest basins, such as the SoG and SJF and smaller differences (0-5 cm) in smaller basins such as those within near Seattle (Fig. 5, Fig. 1). These differences appear to be primarily a result of timing as mean bias between SWM+C and NWM+C are comparatively small (0-2 cm). On average, SWM+C simulations produce slightly higher wave heights resulting in a consistent negative bias across the domain (Fig. 5b).

Prediction errors are also examined for both models. Root-mean-squared-error (RMSE) at three observation sites with data during this period are lower by 1-5 cm for NWM+C predictions compared to SWM+C predictions (Table 4). The largest improvement is observed at 46257 and 46146 both located in larger open basins (Figure 1). Bias at observations sites is relatively similar for NWM+C and SWM+C, within 1-2 cm, and range from -3 to 8 cm (Table 4). Overall, the error with observations is larger than the differences between models suggesting the dominant error terms are not stationary/non-stationary assumptions. While accuracy is improved with non-stationary assumptions, the computational cost of non-stationary simulations were approximately 3x that of stationary simulations.

4.2. Current effects

Over the shorter simulation period (Oct-Nov 2019) stationary simulations (SWM) are compared with and without currents (Table 3). Mean normalized bias (Appendix A.1), SWM+C - SWM, varies from 10-40% with the strongest negative values east and west of Dungeness Spit where depth averaged mean currents show a clockwise circulation pattern (Fig. 6a). Mean wave heights are generally 10-20% higher for SWM+C predictions in the northern part of domain D2 (Fig. 6). Here, the region is sheltered from offshore energy in the SJF by the southern most tip of Vancouver Island. Current refraction is likely increasing the directional spread in wave conditions allowing for additional energy penetration into sheltered regions (Ardhuin et al., 2017). Differences between mean wave heights in domains D3 and D4 are much smaller as currents at these locations are slower (Fig. 6b,c). Similar patterns of Root-mean-squared-differences (RMSD) in wave heights are observed with differences ranging from 0-50% in domain D2 and much less in domains D3 and D4 (Fig. 6).

Prediction errors for SWM and SWM+C at observation sites available during the simulation period are surprisingly similar (Table 4). While SWM+C errors are slightly larger at 46257 this difference is not likely significant. This prediction error similarity is likely because 46257 is at site of strong current shear (Fig. 7). Further study is needed

282 to quantify both the accuracy of current predictions and the potential improvement in prediction accuracy possible by
283 including currents in wave simulations.

284 **4.3. Accuracy at observation locations**

285 Overall predictions during the nearly 5-year simulation period (Table 3) were skilled, with increasingly complex
286 and computationally costly models performing slightly better. Fourteen-day time series at observation locations
287 illustrate some differences and deficiencies (Fig. 8). At locations partially sheltered to offshore wave energy (46088,
288 W1, W2, W3) LSR under-predicted because of the lack of local wind-wave generation (Fig. 8a,i,m,n). At the relatively
289 exposed location, 46257, LSR predictions showed better agreement with observations at most times, but local wind-
290 waves appeared important as well, as indicated by FDL and LUT predictions (Fig. 8d).

291 Modeled wave heights at completely sheltered locations, *i.e.*, not exposed to remote wave energy, were most similar.
292 Predictions in Bellingham and Skagit bays in general show good agreement with observations and between models
293 (SWAN+C, LUT, and FDL) with the exception of locations S1 and S2 where all models were biased low (Fig. 8i,j).
294 Under-predicted wind speeds are suspected as the primary drive of this bias, however, robust wind observations were
295 not available at this location to confirm this hypothesis. In larger basins, such as the SoG and inside the SJF, peak wave
296 heights appeared over-predicted by the LUT approach, but FDL and SWAN+C were similar and more closely aligned
297 with observations (Fig. 8a,b,c).

298 Predictions at 46257 were examined more closely as the site is most exposed to remotely generated energy, while
299 local generation still relatively important. LSR+LUT and LSR+FDL wave height predictions showed good agreement
300 with SWAN+C despite the simplifications employed (Fig. 9a). Overall SWM+C predictions appeared slightly higher
301 during this time period, while LSR+LUT and LSR+FDL appeared more closely aligned with observations. Mean wave
302 period was also well predicted by LSR+LUT and LSR+FDL and showed clearly the oscillation between remotely and
303 locally generated wave conditions (Fig. 9b). Mean wave direction was also well predicted, though it is clear that NW
304 energy both from local winds and offshore waves tend to dominate.

305 Across observation locations SWAN+C and LSR+LUT wave height predictions showed the best agreement with
306 observations (Fig. 10). At most locations LSR+FDL predictions had a negative bias, indicated by quantile-quantile
307 curves (magenta, Fig. 10). At some locations LSR+LUT wave height distributions appeared closest to observations,
308 while at others SWM predictions appeared best. At S1 and S2 a clear negative bias was present for all model
309 configurations, confirming that the observed biases in Fig. 8 were typical throughout the record.

310 Wave height root-mean-squared-error (RMSE) varied across locations but was lowest for SWM+C predictions at
311 most sites (green bars in Fig. 11a). This was similarly true for mean wave periods (Fig. 11b). While LSR+LUT wave
312 height errors were lower than LSR+FDL, mean wave period errors were higher. Larger LSR+LUT RMSE occurred

Table 5

Median RMSE and bias across observations sites for several models (rows) as illustrated in Fig. 11. Median errors/differences are computed with respect to observations (left) and SWM+C predictions (right) and additionally for both all wave conditions ($H_s \geq 0$ m) and solely for relatively large waves ($H_s \geq 0.5$ m). Note that errors at B3 are not included as SWM+C predictions are not available there.

Threshold	Model	Error to observations				Difference to SWM+C			
		H_s [m]		T_m [sec]		H_s [m]		T_m [sec]	
		RMSE	bias	RMSE	bias	RMSD	bias	RMSD	bias
$H_s \geq 0$ m									
	SWM+C	0.17	-0.02	1.2	-0.6	-	-	-	-
	FDL	0.22	-0.07	1.5	-0.9	0.14	0.00	0.7	0.1
	LSR	0.39	-0.27	5.8	5.5	0.33	-0.25	6.7	6.5
	LUT	0.19	-0.03	1.7	-1.1	0.12	0.00	0.8	0.1
	LSR + FDL	0.21	-0.05	1.4	-0.3	0.14	0.00	0.9	0.5
	LSR + LUT	0.17	-0.01	1.7	-0.7	0.12	0.00	0.8	0.1
$H_s \geq 0.5$ m									
	SWM+C	0.31	-0.11	0.7	-0.1	-	-	-	-
	FDL	0.36	-0.27	0.7	-0.2	0.22	-0.11	0.7	0.1
	LSR	0.80	-0.74	5.7	5.5	0.68	-0.64	5.5	5.3
	LUT	0.31	-0.07	0.9	-0.2	0.18	0.04	0.8	0.3
	LSR + FDL	0.34	-0.22	0.8	0.4	0.21	-0.10	0.9	0.8
	LSR + LUT	0.29	-0.07	0.9	-0.2	0.18	0.04	0.7	0.3

313 most strongly at sites 46088, W1, W2, and W3, located just inside the SJF. This appears driven by larger negative
 314 bias in mean wave height prediction (Fig. 11d). Wave height biases varied, but are mostly consistent between models,
 315 suggesting that either models contain a very similar bias or that model forcing biases are driving these errors (Fig.
 316 11c). For example, the largest biases were observed at W1-W3 where small amounts of offshore energy propagation
 317 may be difficult to resolve and highly influence by directional details not resolved well by the directional coefficients
 318 measured by 46087 (Ochoa and Delgado-González, 1990).

319 Median RMSE from all observations sites (except for B3 where SWM+C predictions are not available) for SWM+C
 320 and LSR+LUT were similar (17cm, Table 5). Median RMSE was 21 cm for LSR+FDL and slightly higher for FDL
 321 alone (22cm). Lowest errors for mean period were achieved by SWM+C followed by LSR+FDL. With the exception
 322 of LSR, median bias for wave height and mean period were small as positive bias in some regions tended to cancel
 323 out negative biases in others. Median wave height RMSE in LUT only predictions was relatively low because most
 324 observation sites were not exposed to remote energy. Overall prediction error was low for the combined models,
 325 LSR+FDL and LSR+LUT, and was similar to SWM+C accuracy when averaged across locations and conditions
 326 (17-21 cm wave height RMSE, Table 5). Errors and biases increase when limiting the error analysis to waves conditions
 327 where $H_s \geq 0.5$ m, but the comparison between models stays mainly the same. Surprisingly wave height errors and
 328 bias are slightly lower for LSR+LUT predictions compared to SWM+C, but SWM+C mean period predictions are
 329 still more skilled (Table 5).

330 Mean observed and predicted energy as a function of frequency illustrate where offshore energy and local wind
331 generation tend to dominate observations and predictions (Fig. 12). At 46257, the site most exposed to offshore
332 wave energy, 10-second energy was the largest contributor and was under-predicted by both SWM+C and LSR (Fig.
333 12a). The combined LSR+LUT mean energy predictions agree better with observations than SWM+C predictions
334 that appeared biased high at higher frequency and biased slightly lower at lower frequency. While LSR+LUT
335 appeared best at exposed site 46257, at the mostly sheltered 46088 location mean SWM+C predictions agreed better
336 with observations (Fig. 12b). This is likely due to the LSR predictions underestimating remotely generated energy
337 propagation and the neglected non-linear interactions between remotely and locally generated energy in LSR+LUT. In
338 contrast, results at W1-W3 were more similar for SWM+C and LSR+LUT models (Fig. 12c-e). At sheltered sites the
339 LUT and SWM+C spectral predictions were mostly similar and agree generally with observations. At 46146, mean
340 SWM+C predictions were closer to observations while LUT predictions exceed observed values (Fig. 12f). In larger
341 basin winds are much more likely to be spatially heterogeneous and LUT assumptions will more often be violated. In
342 smaller embayments, such as Bellingham Bay, observations and models agree quite closely with the exception of B3,
343 that is very close to shore and likely not well resolved by the model spatial resolution (Fig. 12h-k).

344 4.4. Model-Model differences

345 In most cases, model-model differences are smaller than model errors with observations. Root-mean-squared-
346 differences (RMSD) are estimated between SWM+C, and LSR+FDL and LSR+LUT models at observation locations
347 and shown in red outlines in Fig. 11a,b. With the exception of S1-S3, wave height and mean period errors between these
348 reduced-physics models (LSR+FDL, LSR+LUT) and SWM+C are lower than errors with the observations themselves.
349 This suggests that either the models are prone to errors in very similar ways, or that uncertainty in the model forcing
350 dominates prediction error (*e.g.*, biases in wind predictions, errors in bathymetry, or poorly resolved directional wave
351 spectra offshore). Results are similar for model biases, but less consistent, and in some locations model-model bias
352 and mode-observation is similar. Median RMSD and bias across observation sites are consistent with these findings
353 indicating that model-model differences are generally lower than model errors to observations (Table 5).

354 While observation sites are sparsely dispersed across the domain, model-model comparisons illustrate differences
355 spatially across the complex region. Owing to data constraints, spatial outputs were compared over the shorter 2-month
356 time period during October and November of 2019. Mean wave heights during this time vary between models, but are
357 similar for SWM+C and LSR+LUT predictions (Fig. 13a-d). Mean bias between simplified models and SWM+C
358 shows clearly where offshore energy (LSR) and locally generated energy (LUT) dominate (Fig. 13e,f). In the SJF
359 bias between LSR and SWM+C is relatively small, up to 0-30% of the mean wave height while root-mean-squared-
360 differences (RMSD) normalized by mean SWM+C wave heights (Fig. 13a) are 0-50% (Fig. 13e,h). In the SoG and

361 protected part of Puget Sound errors and bias between SWM+C and LUT are small, 10-30%. The combined model,
362 LSR+LUT, misfit to SWM+C is relatively small in most places, with bias and RMSDs just 10-20% of the mean wave
363 height. Some exceptions are observed in narrow bays and inlets where SWM+C spatial resolution was too coarse to
364 resolve wave generation (Table 2). It is likely the higher resolution LUT predictions more correctly represent wave
365 conditions in these locations.

366 In the lee of Vancouver Island (eastward), just inside the SJF, LSR+LUT predicted wave height are slightly smaller
367 (10-30%) than SWM+C, appearing to diffuse less northward energy into basin. The north-south gradient caused by
368 the sheltering by Vancouver island is sharper for LSR+LUT than for SWM+C. While diffraction is not used in any
369 models, non-linear wave-wave interactions not captured in LSR+LUT may increase directional spreading breaking
370 down sharp sheltering gradients. Additionally, model spatial and directional resolutions vary significantly and model
371 numerics may also be responsible for reducing gradients in comparatively coarser resolutions.

372 4.5. Trade-offs

373 Non-stationary SWAN simulations, at the spatial resolution needed to resolve details of a domain such as the
374 Salish Sea, are currently impractical for long-term simulations. While the use of unstructured grids has allowed for
375 some progress (Yang et al., 2019) it is unclear whether sheltering details in the SJF are properly resolved or if such a
376 method is practical for much longer simulations. The relatively short (2-month) non-stationary simulations presented
377 here required 9 days to complete on a 2 Intel® Xeon® Processor E3-1276 v3 nodes (4-cores each), a computational
378 cost approximately 3x that of comparable stationary simulations. This 3x increase in required expense reduced wave
379 height errors by a relatively modest 1-2 cm at 46257 and Spot-1 observation sites (Table 4) and exhibited relatively
380 small root-mean-squared-differences of 0-10cm between models across the domain (Fig. 5c).

381 While comparatively faster, 5-year stationary simulations (SWM+C) required 14 days to complete on 12 nodes
382 (4-cores each), for many, this represents an insignificant computational cost. In addition, traditional SWAN imple-
383 mentations must be run again to revise predictions if input forcing is updated or modified. This is not uncommon
384 in climate change scenario downscaling where new global forcings become available with each iteration of model
385 development. Typically these simulations are long (100+ years), and have multiple scenarios, *e.g.*, representative
386 concentration pathways (RCPs). A significant advantage of the rapid approaches presented here (FDL, LSR, and LUT)
387 is the insignificant computational cost of producing updated predictions after required simulations are completed.

388 Though not insignificant, the construction of the LUT suite of simulations (1,728 in total) required approximately
389 30 days to complete on one Intel Ivy Bridge node (20-cores), about 1/2 of the compute time required by the 5-
390 year stationary model (SWM+C). Albeit, computational expense is not directly comparable between the two due
391 to difference in IT-infrastructure. SWAN simulations required by LSR transformation estimates was comparatively

392 trivial, running overnight on a 12-core desktop machine. FDL predictions required the most trivial computational cost
393 as no numerical simulations were needed. For all of these methods, the initial computation was needed only once. Once
394 simulations were completed, predictions were rapidly made for any set of forcing conditions (5-year interpolations can
395 be completed in minutes).

396 At observation sites considered here, RMSE of LSR+LUT and LSR+FDL methods were within 4 cm and 0.5
397 seconds of SWM+C errors for wave height and mean period, respectively. Normalized bias and RMSD between
398 these reduced-physics models and SWM+C range from 0-30% in most of the regions. In terms of absolute error
399 to observations, the relative gain in accuracy with a traditional SWAN implementation was found to be considerably
400 small. Differences between models varied over the region. In modestly sized bays with minimal exposure to remotely
401 generated waves differences were quite small. While larger differences were observed in more dynamic regions such
402 as the SJF (Fig. 7), without additional observations, conclusions about absolute errors and improvement can not made.

403 In addition to computational savings, LSR and LUT approaches allow for higher spatial resolution than what is
404 practical in traditional SWAN implementations. While resolution varied from 50-1,000 meters in nested SWM+C
405 domains, LSR and LUT predictions were made on 50-m and 100-m resolution grids across the Puget Sound (L2) and
406 larger Salish Sea region (L1, LSR, Table 2) with the potential to resolve nearshore wave conditions more accurately.

407 Overall these rapid approaches reduce computation cost by 2-4 orders of magnitude while incurring a relatively
408 small loss in accuracy (Table 5), that may be larger in highly dynamic regions. Implementation is relatively
409 straightforward, but more complex than traditional model building. Such rapid frameworks excel most strongly where
410 high resolution and very long predictions are required.

411 5. Summary

412 In the Salish Sea region stationary SWAN assumptions result in only minor skill degradation (Table 4). SWAN
413 simulations show that while including currents effects had negligible impact to skill at observation sites available
414 (Table 4), spatial wave are likely significantly effected in the SJF near Dungeness Spit (Fig. 6).

415 Overall, rapid implementations of fetch-limited, look-up-table, and linear spectral refraction are skill-full in much
416 of the region as compared to traditional SWAN simulations (Table 5). Combinations of these methods appear to capture
417 both remotely and locally generated waves well, despite missing non-linear interactions between them. Additionally,
418 model-model comparisons show lower root-mean-squared-differences than compared with observations (Fig. 11)
419 suggesting that prediction error may be due to uncertainties in model boundary forcing, *e.g.*, errors in wind predictions,
420 uncertainties in directional details of offshore waves, and errors in bathymetry.

421 The rapid approaches presented here may server as a framework for rapid coastal prediction where local, remote,
422 or both types of wave energy are prevalent. The methods require orders of magnitude (2-4) less computation than

423 traditional SWAN implementations and are well suited to support both rapid near-term forecast systems and long-term,
424 high-resolution, historical or future simulations needed to evaluate robust wave statistics alongshore.

425 A. Appendix

426 A.1. Error Metrics

The error metrics used throughout are defined here. Mean bias is defined as,

$$\text{bias} = \frac{1}{T} \sum_{i=1}^T (p_i - o_i), \quad (10)$$

where predictions, p , and observations, o , are taken from each valid time step, i . Similarly, Root-Mean-Square-Error (RMSE) is estimated by,

$$\text{RMSE} = \sqrt{\frac{1}{T} \sum_{i=1}^T (p_i - o_i)^2}. \quad (11)$$

Normalized metrics are estimated by dividing by mean values after computation rather than determining mean errors from normalized values at each time-step. These definitions weight larger values more heavily, ignoring large relative errors during periods of low energy. Here, normalized-bias (Nbias) is defined as,

$$\text{Nbias} = 100 \cdot \frac{\frac{1}{T} \sum_{i=1}^T (p_i - o_i)}{\frac{1}{T} \sum_{i=1}^T o_i}, \quad (12)$$

and normalized-root-mean-squared-error (NRMSE) is defined as

$$\text{NRMSE} = 100 \cdot \frac{\sqrt{\frac{1}{T} \sum_{i=1}^T (p_i - o_i)^2}}{\frac{1}{T} \sum_{i=1}^T o_i}. \quad (13)$$

427 Here, errors are considered as the difference between model and observations. Additionally we consider the difference
428 between models, such as the bias and normalized-root-mean-squared-difference (RMSD). These consider same formula
429 above, but swap o with some reference model prediction, *e.g.*, p_{ref} . Here the reference model is typically the more
430 complex model, where the goal is to determine what is missing, error-wise, in the simplified model.

431 A.2. Fetch-depth-limited optimization

432 FDL predictions can be made rapidly, and with two free parameters, α and β , may be optimized. Here, LSR
433 predictions are added (LSR+FDL) for locations exposed to remotely generated energy. Wave height RMSE vary
434 for LSR+FDL predictions over a range of α and β values (Fig. A1). Optimal α and β values minimize wave height

435 RMSE and are indicated by red circles in Fig. A1 at varying observation location. Optimal values were not consistent
 436 between observation locations (Table 1). Despite occupying similar large basins without offshore wave exposure, lowest
 437 RMSEs at 46146 were observed with small β values while 46131 indicated a larger β yielded better skill (Fig. A1b,c).
 438 Observations in Bellingham Bay (B1-B3) show similar disagreement for preferred α and β values.

439 The observed lack of agreement of optimal α and β values, even in similar locations, suggest that these parameters
 440 are compensating for wind forcing uncertainties or limitations of the empirical method itself. Additionally, while
 441 here wind input is taken at the nearest over-water prediction location to the prediction location, a more sophisticated
 442 approach would be take a weighted average of up-wind wind conditions, and an optimization of plausible weight
 443 parameters may yield more consistent results. Nonetheless, for simplicity, here errors were averaged across all sites
 444 and an optimal average value of $\beta = 1$ and $\alpha = 1$ (Fig. A1o) was therefore used in the following analysis across the
 445 region.

446 **CRedit authorship contribution statement**

447 **Sean C. Crosby:** Model framework development, implementation, analysis, and study design. **Cornelis M.**
 448 **Nederhoff:** Coupled model development and implementation. **Nathan VanArendonk:** High performance computer
 449 model simulations. **Eric E. Grossman:** Wrote funding proposal, lead larger effort.

450 **References**

- 451 Arduin, F., Gille, S. T., Menemenlis, D., Rocha, C. B., Rasche, N., Chapron, B., Gula, J., and Molemaker, J. (2017). Small-scale open ocean currents
 452 have large effects on wind wave heights. *Journal of Geophysical Research: Oceans*, 122:4500–4517.
- 453 Battalio, B., Chandrasekera, C., Divoky, D., Hatheway, P. D., Hull, C. T., Bill, P. O., Seymour, D., Srinivas, P. R., and Hatheway, D. D. D. (2005).
 454 Wave transformation: Fema coastal flood hazard analysis and mapping.
- 455 Booij, N., Ris, R. C., and Holthuijsen, L. H. (1999). A third-generation wave model for coastal regions: 1. model description and validation. *Journal*
 456 *of Geophysical Research*, 104:7649–7666.
- 457 Camus, P., Mendez, F. J., and Medina, R. (2011). A hybrid efficient method to downscale wave climate to coastal areas. *Coastal Engineering*,
 458 58:851–862.
- 459 Camus, P., Mendez, F. J., Medina, R., Tomas, A., and Izaguirre, C. (2013). High resolution downscaled ocean waves (dow) reanalysis in coastal
 460 areas. *Coastal Engineering*, 72:56–68.
- 461 Canada, E. (2019). Historic hydrometric data extracted from the environment and climate change canada historical hydrometric data web site. Date
 462 Accessed: Dec 2020.
- 463 CERC (1984). Shore protection manual book ii.
- 464 Crosby, S. C. and Grossman, E. E. (2019). Wave observations from nearshore bottom-mounted pressure sensors in skagit and bellingham bays,
 465 washington, usa from dec 2017 to feb 2018.
- 466 Crosby, S. C., Kumar, N., O'Reilly, W. C., and Guza, R. T. (2018). Regional swell transformation by backward ray tracing and swan. *Journal of*
 467 *Atmospheric and Oceanic Technology*, 36:217–229.

- 468 Crosby, S. C., O'Reilly, W. C., Guza, R. T., Crosby, S. C., O'Reilly, W. C., and Guza, R. T. (2016). Modeling long-period swell in southern california:
469 Practical boundary conditions from buoy observations and global wave model predictions. *Journal of Atmospheric and Oceanic Technology*,
470 33:1673–1690.
- 471 Dorrestein, R. (1960). Simplified method of determining refraction coefficients for sea waves. *Journal of Geophysical Research*, 65:637–642.
- 472 Elliott, A. J. and Neill, S. P. (2015). Simulating storm waves in the irish sea. <http://dx.doi.org/10.1680/maen.2007.160.2.57>, 160:57–64.
- 473 Erikson, L. H., Hegermiller, C. A., Barnard, P. L., Ruggiero, P., and van Ormondt, M. (2015). Projected wave conditions in the eastern north pacific
474 under the influence of two cmip5 climate scenarios. *Ocean Modelling*, 96:171–185.
- 475 Finlayson, D. (2006a). The geomorphology of puget sound beaches. *Puget Sound Nearshore Partnership / University of Washington, Seattle*.
- 476 Finlayson, D. P. (2006b). The geomorphology of the puget sound beaches. Tides are mixed semidiurnal, near 180-deg phase relationship between
477 diurnal and semidiurnal results in two nearly equal high tides and extreme low tide, this leads to water level assymetry in tidal levels.
NTR
478 = obs - pred. Wrong. This leads to incorrect estimates of NTR extreme probabilities per month. Additionally yearly averages of slp and tide level
479 lead to 19.4 mm/mb. I could not replicate this. My estimates are much lower with properly filtered observations.
- 480 Gallet, B. and Young, W. R. (2014). Refraction of swell by surface currents. *Journal of Marine Research*, 72:105–126.
- 481 García-Medina, G., Özkan Haller, H. T., Ruggiero, P., and Oskamp, J. (2013). An inner-shelf wave forecasting system for the u.s. pacific northwest.
482 *Weather and Forecasting*, 28:681–703.
- 483 Golshani, A. A. (2011). A 60 years wave hindcast study in the south of persian gulf using swan model & semi-time domain method. *Journal Of*
484 *Marine Engineering*, 6:73–87.
- 485 Hasselmann, K., Barnett, T. P., Bouws, E., Carlson, H., Cartwright, D. E., Enke, K., Ewing, J. A., Gienapp, H., Hasselmann, D. E., Kruseman, P.,
486 Meerburg, A., Muller, P., Olbers, D. J., Richter, K., Sell, W., and Walden, H. (1973). Measurements of wind-wave growth and swell decay during
487 the joint north sea wave project (jonswap). *Erganzungsheft zur Deutschen Hydrographischen Zeitschrift Reihe, A*(8):p.95.
- 488 Hegermiller, C. A., Rueda, A., Erikson, L. H., Barnard, P. L., Antolinez, J. A. A., and Mendez, F. J. (2017). Controls of multimodal wave conditions
489 in a complex coastal setting. *Geophysical Research Letters*, 44:12,315–12,323.
- 490 Hegermiller, C. A., Warner, J. C., Olabarrieta, M., and Sherwood, C. R. (2019). Wave–current interaction between hurricane matthew wave fields
491 and the gulf stream. *Journal of Physical Oceanography*, 49(11):2883–2900.
- 492 Jones, N. L. and Monismith, S. G. (2007). Measuring short-period wind waves in a tidally forced environment with a subsurface pressure gauge.
493 *Limnology and Oceanography: Methods*, 5:317–327.
- 494 Kernkamp, H. W., Van Dam, A., Stelling, G. S., and De Goede, E. D. (2011). Efficient scheme for the shallow water equations on unstructured grids
495 with application to the Continental Shelf. *Ocean Dynamics*, 61(8):1175–1188.
- 496 Kumar, N., Cahl, D. L., Crosby, S. C., and Voulgaris, G. (2017). Bulk versus spectral wave parameters: Implications on stokes drift estimates,
497 regional wave modeling, and hf radars applications. *Journal of Physical Oceanography*, 47:1413–1431.
- 498 Lambrakos, K. F. (1981). Wave-current interaction effects on water velocity and surface wave spectra. *Journal of Geophysical Research*, 86:10955.
- 499 Leijnse, T., van Ormondt, M., Nederhoff, K., and van Dongeren, A. (2021). Modeling compound flooding in coastal systems using a computationally
500 efficient reduced-physics solver: Including fluvial, pluvial, tidal, wind- and wave-driven processes. *Coastal Engineering*, 163:103796.
- 501 Longuet-Higgins, M., Cartwright, D., and Smith, N. (1963). Observations of the directional spectrum of sea waves using the motions of a floating
502 buoy. In *Proceedings of the Royal Society of London. Series A, Mathematical and Physical Sciences*, pages 111–136.
- 503 Longuet-Higgins, M. S. (1957). On the transformation of a continuous spectrum by refraction. *Mathematical Proceedings of the Cambridge*
504 *Philosophical Society*, 53:226.

- 505 Lyard, F., Carrere, L., Cancet, M., Guillot, A., and Picot, N. (2017). Fes2014, a new finite elements tidal model for global ocean. *Ocean Dynam.*,
506 *in preparation*, 10.
- 507 Lygre, A. and Krogstad, H. E. (1986). Maximum entropy estimation of the directional distribution in ocean wave spectra. *Journal of Physical*
508 *Oceanography*, 16:2052–2060.
- 509 Mehaute, L. B., Wang, J. D., Mehaute, B. L., and Wang, J. D. (1982). Wave spectrum changes on sloped beach. *Journal of the Waterway, Port,*
510 *Coastal and Ocean Division*, 108:33–47.
- 511 Munk, W. H., O'Reilly, W. C., and Reid, J. L. (1988). Australia-bermuda sound transmission experiment (1960) revisited. *Journal of Physical*
512 *Oceanography*, 18:1876–1898.
- 513 Ochoa, J. and Delgado-González, O. E. (1990). Pitfalls in the estimation of wind wave directional spectra by variational principles. *Applied Ocean*
514 *Research*, 12:180–187.
- 515 O'Reilly, W. and Guza, R. (1993). A comparison of two spectral wave models in the southern california bight. *Coastal Engineering*, 19:263–282.
- 516 O'Reilly, W., Olfé, C. B., Thomas, J., Seymour, R., and Guza, R. (2016). The california coastal wave monitoring and prediction system. *Coastal*
517 *Engineering*, 116:118–132.
- 518 O'Reilly, W. C. and Guza, R. T. (1991). Comparison of spectral refraction and refraction-diffraction wave models. *Journal of Waterway, Port,*
519 *Coastal, and Ocean Engineering*, 117:199–215.
- 520 O'Reilly, W. C., Herbers, T. H. C., Seymour, R. J., and Guza, R. T. (1996). A comparison of directional buoy and fixed platform measurements of
521 pacific swell. *Journal of Atmospheric and Oceanic Technology*, 13:231–238.
- 522 Survey, U. G. (2016). National water information system data available on the world wide web (usgs water data for the nation). Date Accessed: Dec
523 2020.
- 524 Sweet, W., Hamlington, B., Kopp, R., Weaver, C., Barnard, P., Bekaert, D., Brooks, W., Craghan, M., Dusek, G., Frederikse, T., Garner, G., Genz,
525 A., Krasting, J., Larour, E., Marcy, D., Marra, J., Obeysekera, J., Osler, M., Pendleton, M., Roman, D., Schmied, L., Veatch, W., White, K., and
526 Zuzak, C. (2022). Global and regional sea level rise scenarios for the united states. *Technical Report NOS 01. National Oceanic and Atmospheric*
527 *Administration, National Ocean Service, Silver Spring, MD*, page 111.
- 528 Tehranirad, B., Crosby, S., Stevens, A. W., Grossman, E. E., VanArendonk, N., Nowacki, D., Nederhoff, K., Erikson, L., and Barnard, P. (2023).
529 Extreme water levels in the salish sea: A new method to simulate sea level anomalies. *Ocean Modeling, in review*.
- 530 Thompson, R. E. and Thomson, R. E. (1994). Physical oceanography of the strait of georgia-puget sound-juan de fuca strait system. In *Symposium*
531 *on the Marine Environment*, volume 1948, pages 36–100.
- 532 Tyler, D., Danielson, J., Grossman, E., and Hockenberry, R. (2020). Topobathymetric model of puget sound, washington, 1887 to 2017. *Science*
533 *Base*.
- 534 Tyler, D., Danielson, J., Grossman, E., and R.J., . H. (2021). Topobathymetric model of the strait of juan de fuca, 1891 to 2016. *Science Base*.
- 535 USGS Advanced Research Computing, U. Y. S. U. G. S. (2021). <https://doi.org/10.5066/f7d798mj>.
- 536 W. J., G., Brunengo, M. J., Jr., W. S. L., Logan, R. L., Shipman, H., and Walsh, T. L. (1997). Puget sound bluffs: The where, why, and when of
537 landslides following the holiday 1996/97 storms. *Washington Geology*, 25.
- 538 Yang, Z., García-Medina, G., Wu, W. C., Wang, T., Leung, L. R., Castrucci, L., and Mauger, G. (2019). Modeling analysis of the swell and wind-sea
539 climate in the salish sea. *Estuarine, Coastal and Shelf Science*, 224:289–300.
- 540 Young, I. and Verhagen, L. (1996). The growth of fetch limited waves in water of finite depth. part 1. total energy and peak frequency. *Coastal*
541 *Engineering*, 29:47–78.

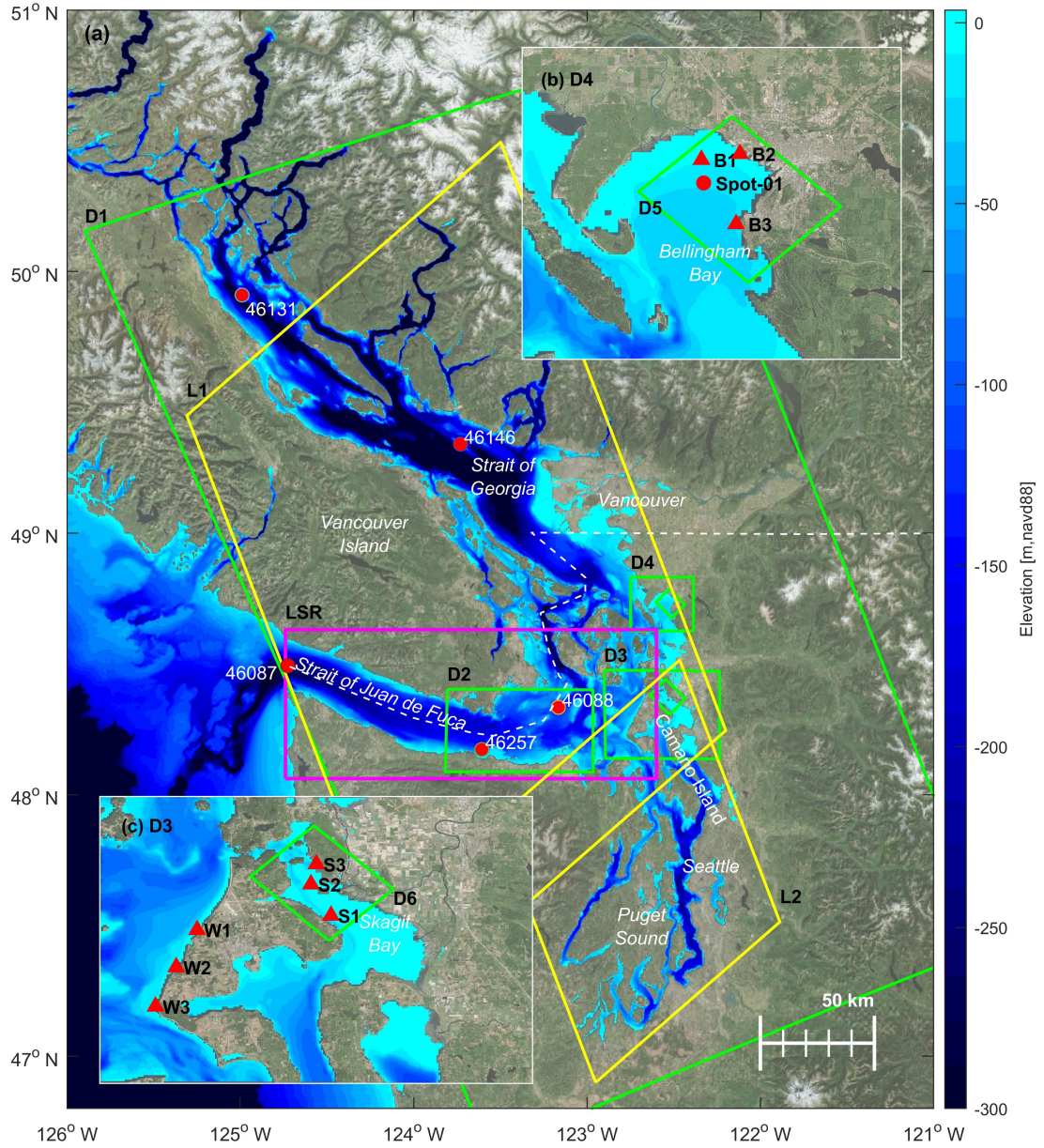


Figure 1: Bathymetry, observation locations, and wave model domains (Table 2) in the Salish Sea. Domain grid extents are shown in green (SWM), magenta (LSR), and yellow (LUT) and labeled in black bold. Wave buoy locations are shown by filled red circles and bottom-mounted pressure sensors by red filled triangles (Table 1). Subsets (b) and (c) are zoomed to SWAN domains D4 and D3, respectively. Dashed white line shows international border between Canada and the United States

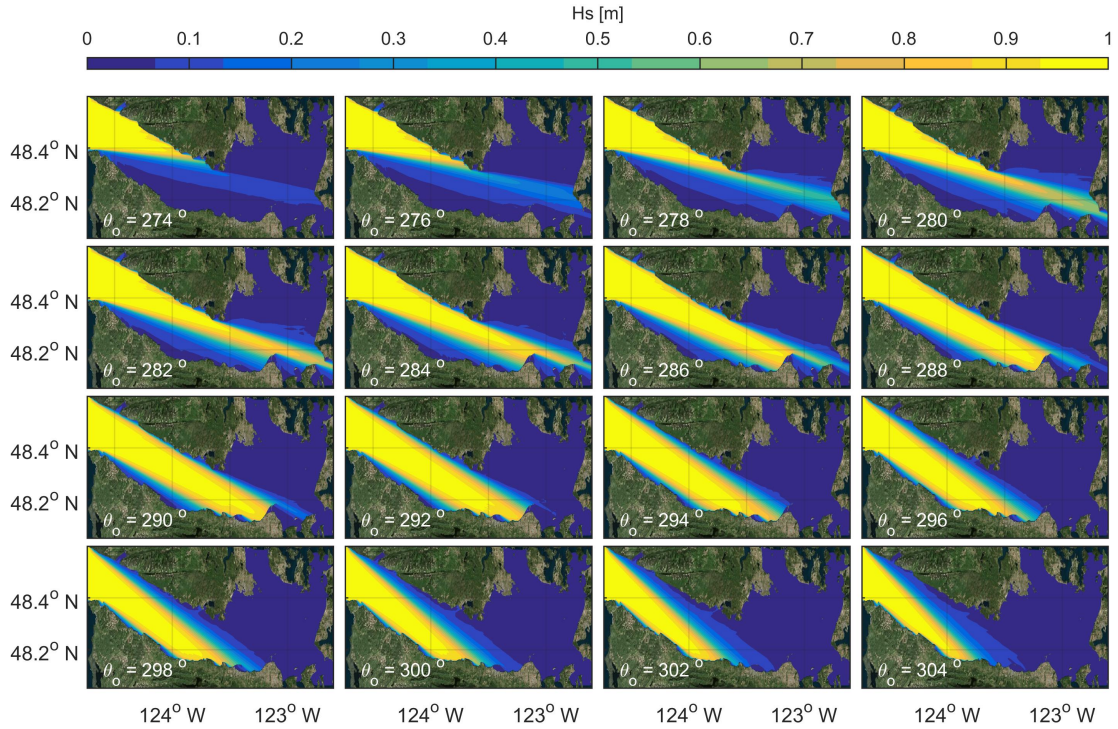


Figure 2: Linear Spectral Refraction (LSR) model runs for a selection of incoming wave directions (θ_o , black text). Wave heights are shown in color. Note that simulations are computed from 180° - 360° at 2° increments and incoming wave energy is evenly distributed across frequency bands (0.04 – 0.5 Hz).

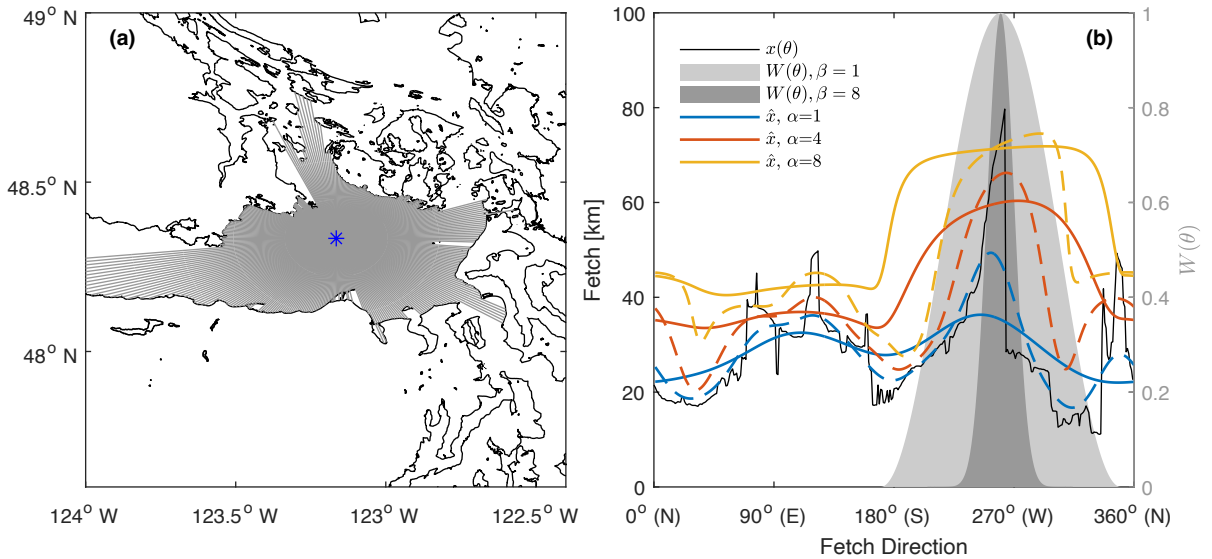


Figure 3: (a) Rays (grey) traced from Hein bank (blue asterisk) at 1° direction intervals terminating at land determine fetch extent. (b) Fetch (solid black) versus fetch direction. Effective fetch, \hat{x} , is shown with varying α (colors, see legend) and for $\beta = 1$ (solid lines) and $\beta = 16$ (dashed lines). The weighting function, $W(\theta)$, is illustrated in light gray for $\beta = 2$ and dark gray for $\beta = 16$ shading with scaling on the right-hand y-axis.

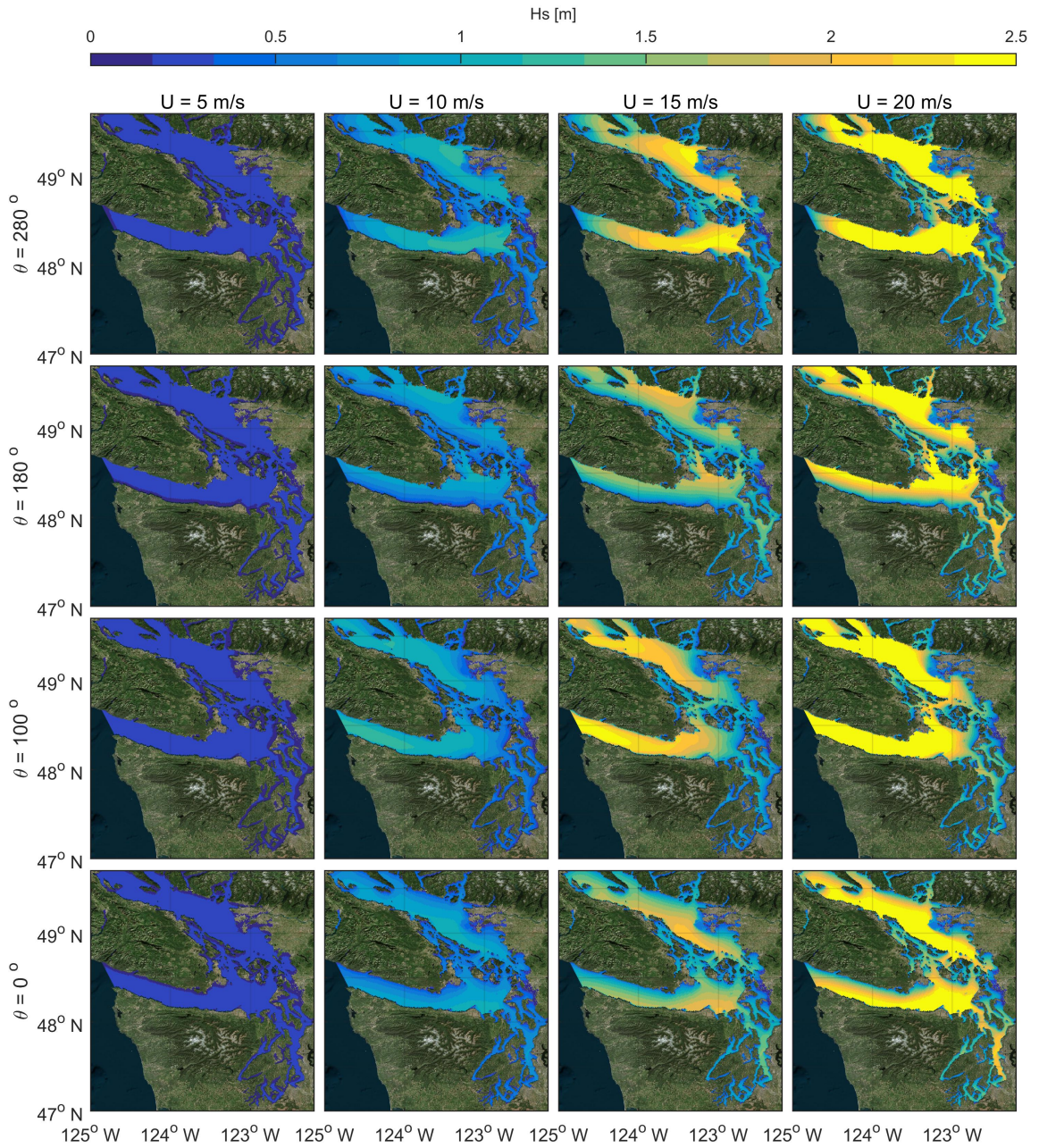


Figure 4: Wave heights for several Look-up-table (LUT) model runs for varying wind speeds (columns) and wind directions (rows).

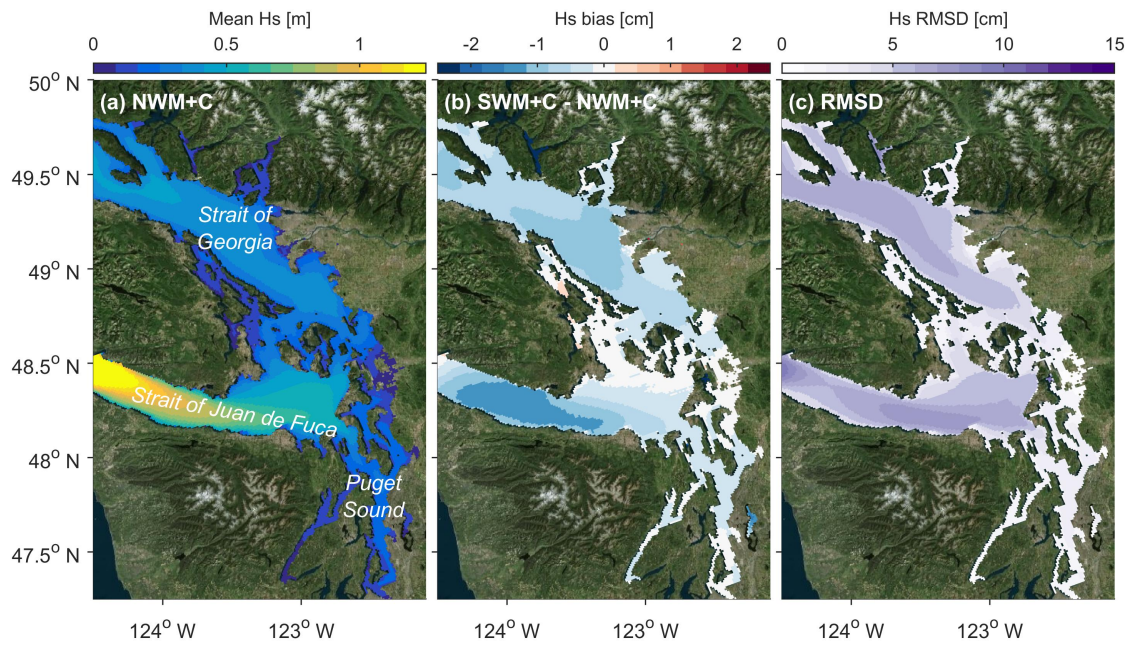


Figure 5: (a) Non-stationary (NWM+C) mean modeled wave heights from Oct 1 2020 through Nov 30 2020. Mean wave height bias, (b), and root-mean-squared-difference, (c), between stationary (SWM+C) and non-stationary simulations (SWM+C - NWM+C).

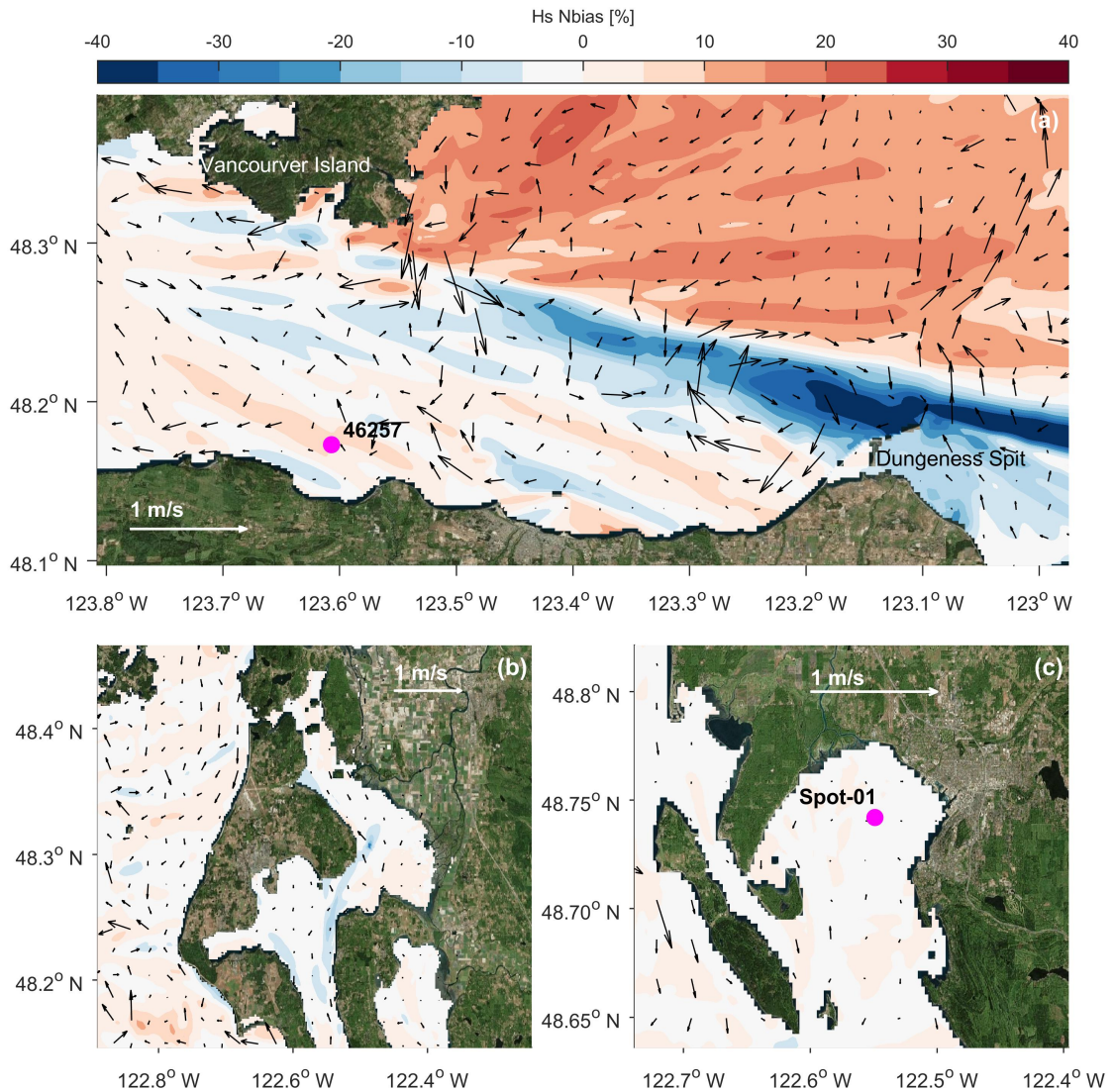


Figure 6: Normalized wave height bias (Nbias, see appendix A.1) between stationary runs with currents (SWM+C) and without (SWM) predictions for domains (a) D2, (b) D3, and (c) D4 (Table 2) for predictions from October to November 2020. Black arrows show mean depth-averaged current velocity with white arrow and text providing scale. Magenta circles show locations wave buoys (Table 1).

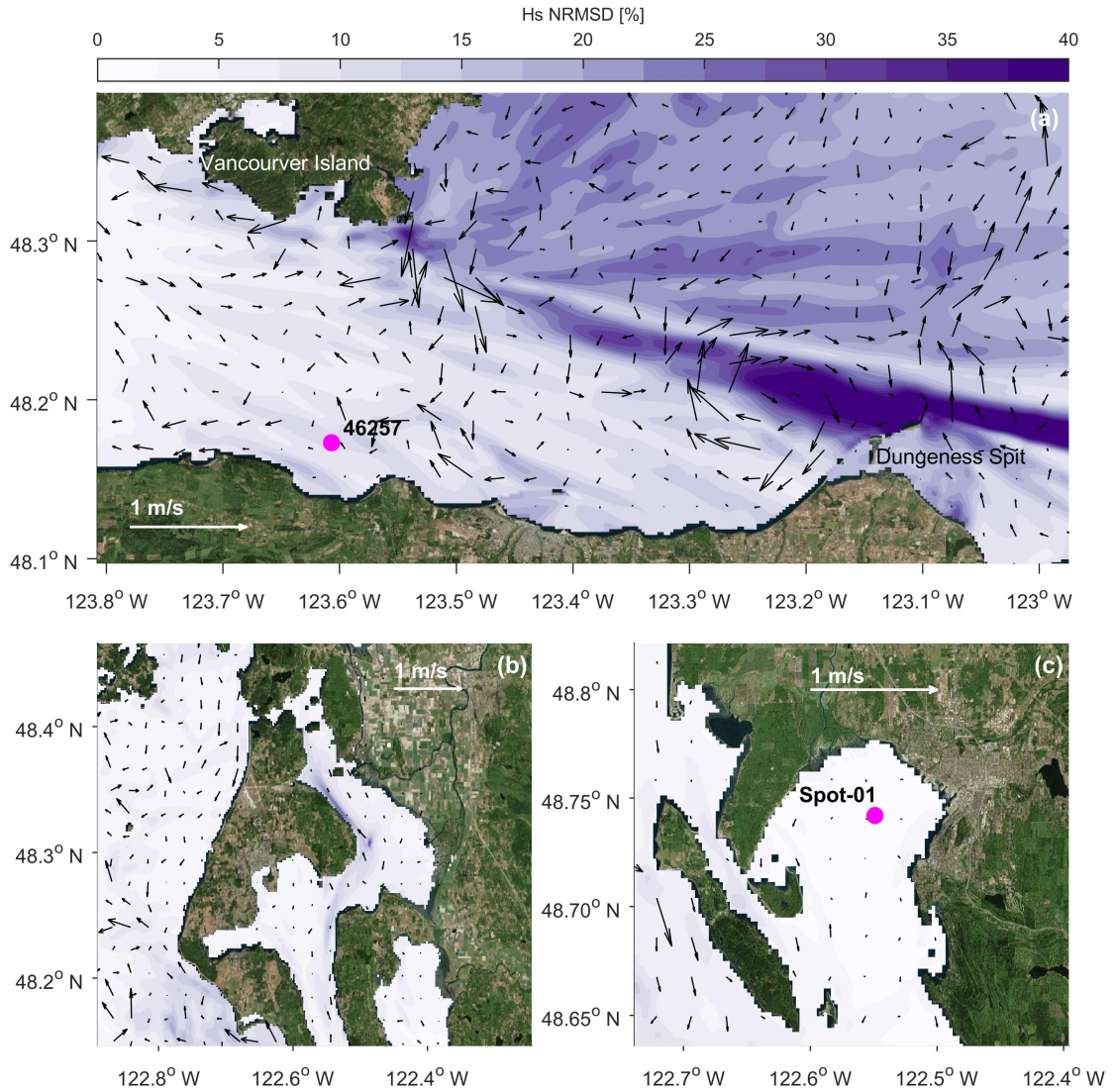


Figure 7: Normalized root-mean-squared-difference (NRMSD, see appendix A.1) between stationary with currents (SWM+C) and without (SWM) predictions for domains (a) D2, (b) D3, and (c) D4 (Table 2) for predictions from October to November 2020. Black arrows show mean depth-averaged current velocity with white arrow and text providing scale. Magenta circles show locations wave buoys (Table 1).

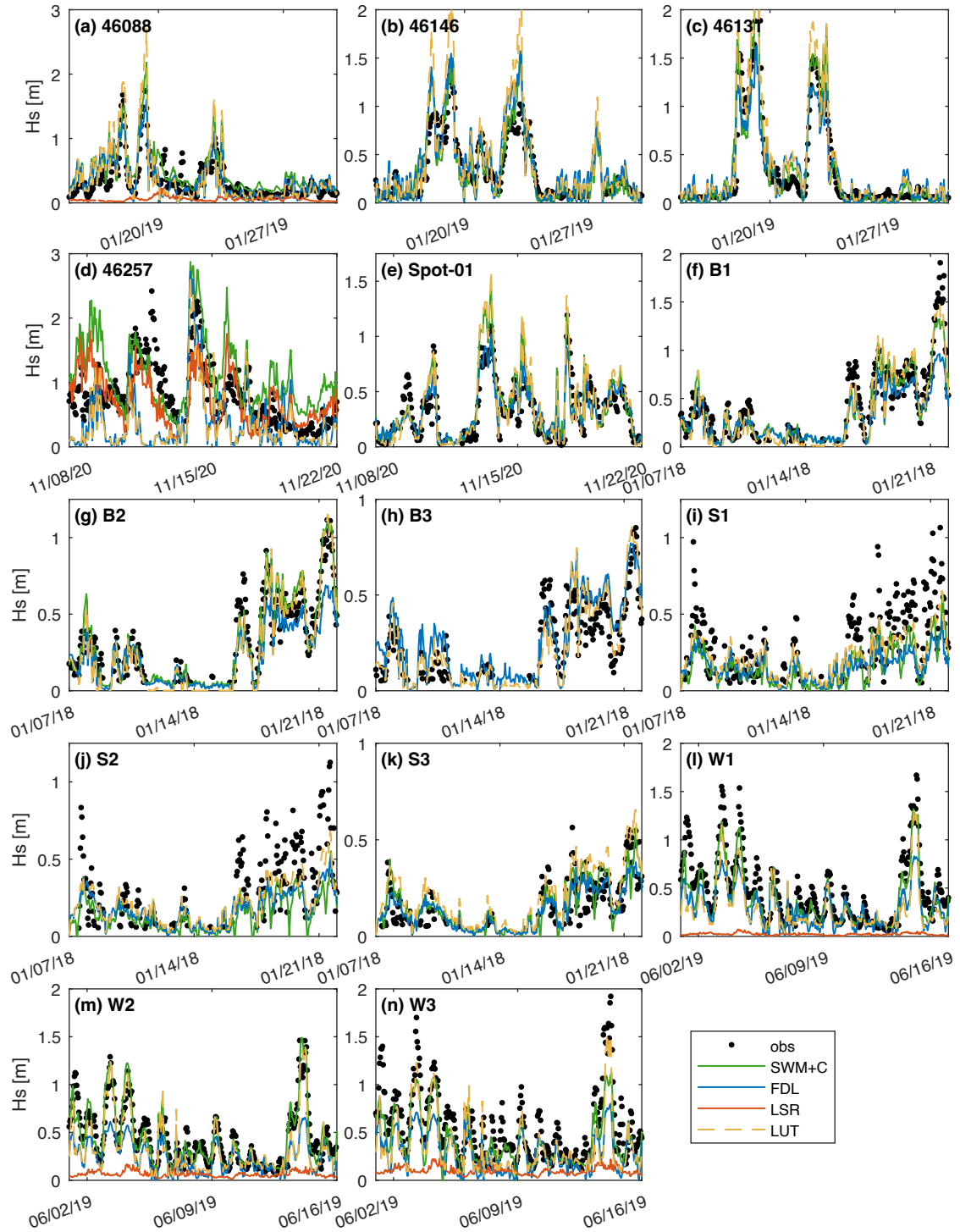


Figure 8: Model-predicted (colors) and observed (black dots) wave heights versus time at varying buoy locations (a-n) for varying model configurations (see legend). Note, LSR predictions are only made at sites exposed to offshore waves, and SWM+C predictions not available at B3 due to its close proximity to land.

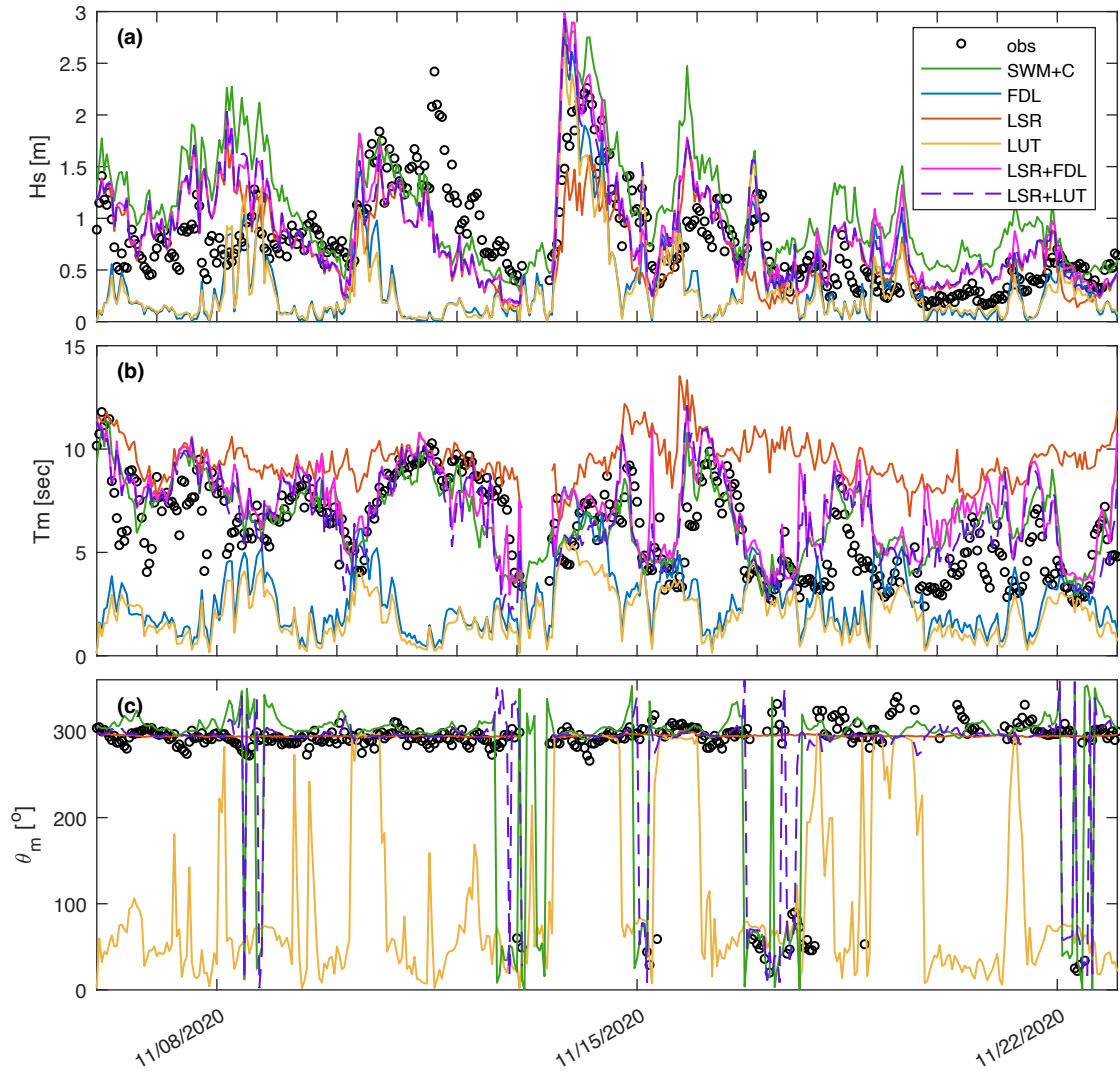


Figure 9: Model-predicted (colors) and observed (black dots) wave heights (a), mean periods (b), and mean direction (c) versus time at buoy 46257 for varying model configurations (see legend). Note FDL and FDL+LUT mean direction are not shown because the FDL approach does not include a directional component.

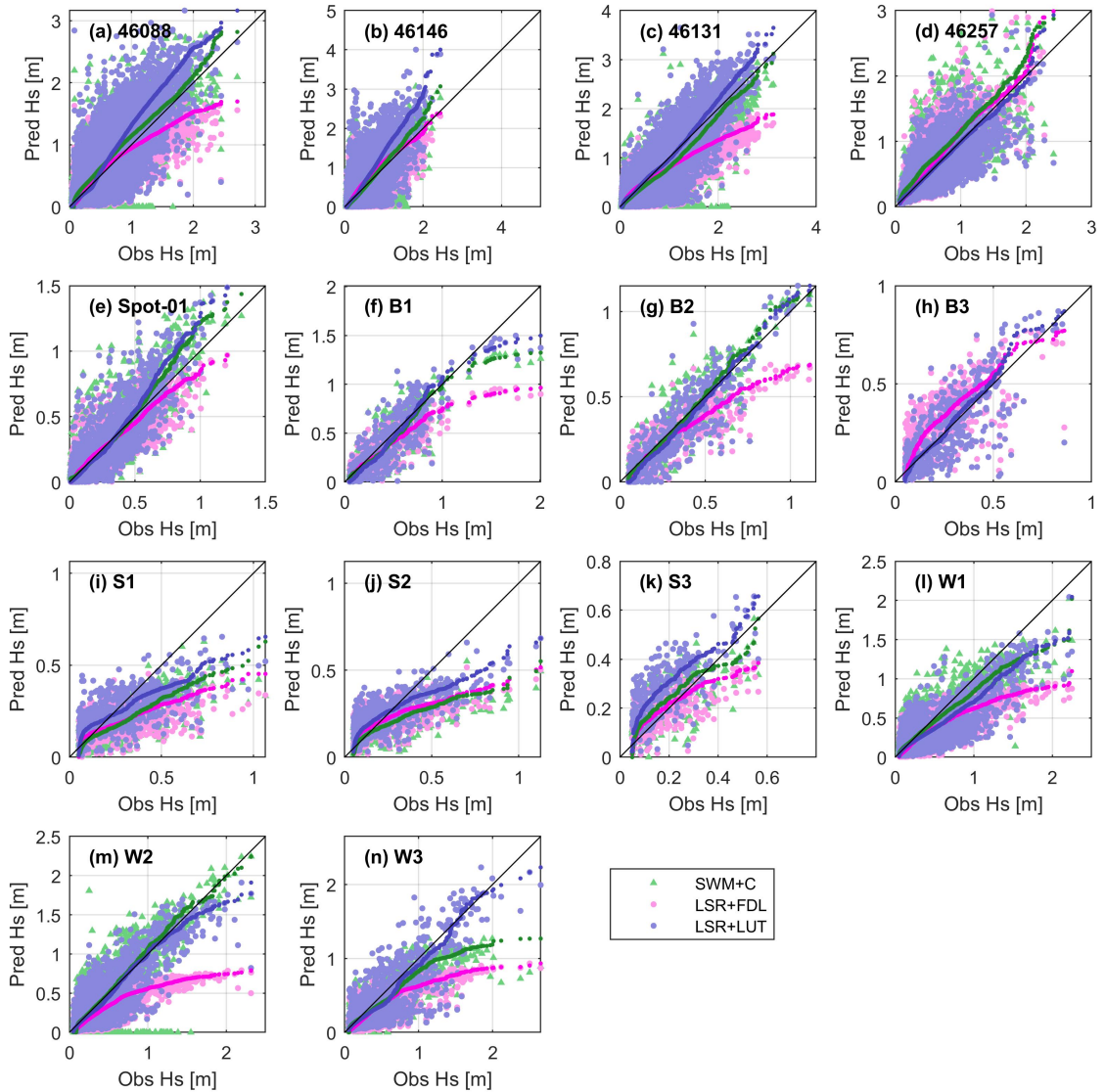


Figure 10: Quantile-quantile (q-q) plots of observed (x-axis) and model-predicted (y-axis) wave height. Different colors represent different model configurations with lighter colors depicting observations and darker colors their quantiles. In particular, stationary swan with current (SWM+C), LSR+FDL and LSR+LUT are shown.

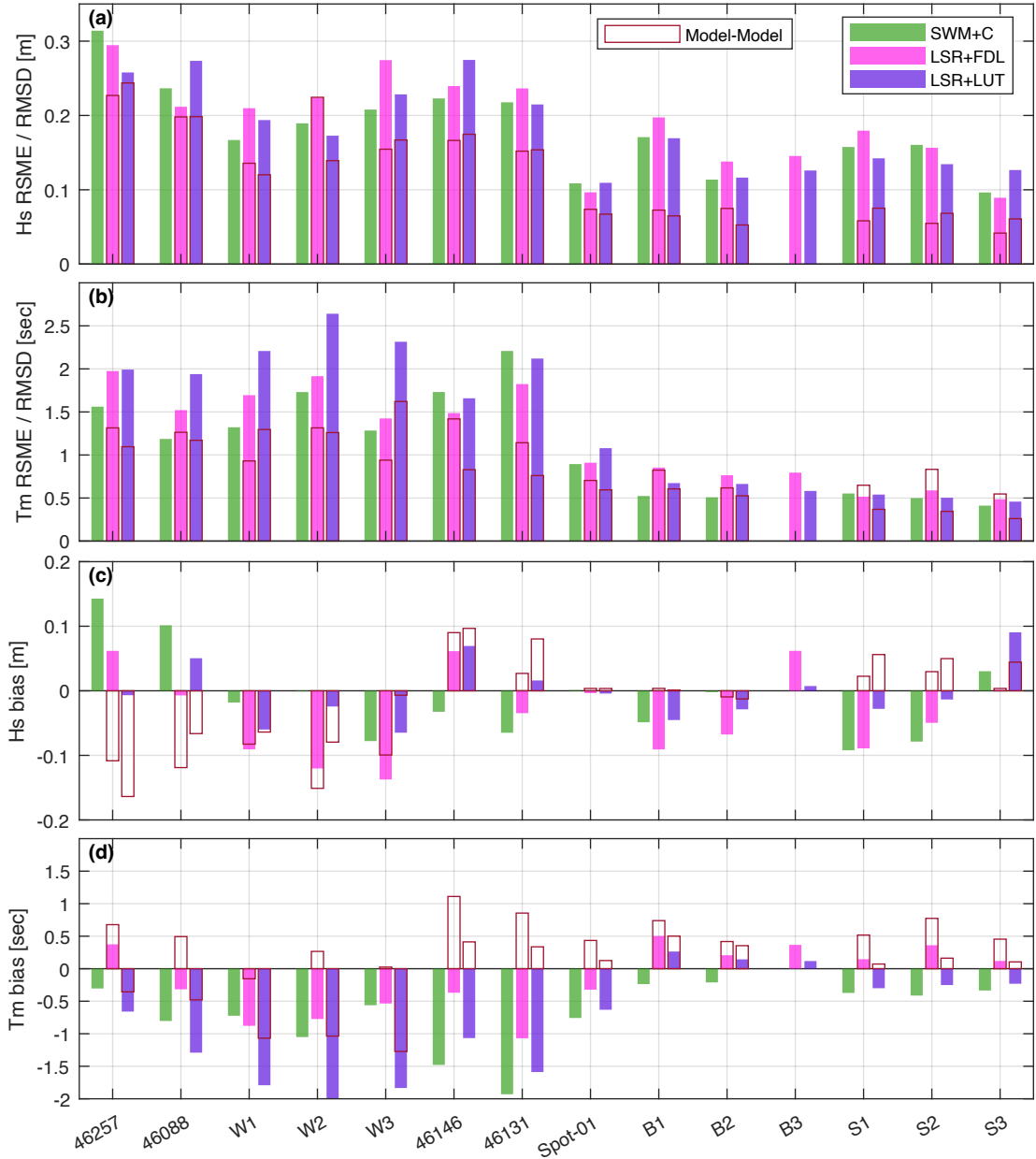


Figure 11: Root-mean-square-error (RMSE) and bias of predicted wave heights (a,c) and mean periods (b,d) versus observation location for varying model configurations (see legend). Dark red outlines show root-mean-squared-difference (RMSD) and bias between the outlined model and SWAN+C, illustrating relative magnitude of model-model error to model-observation error.

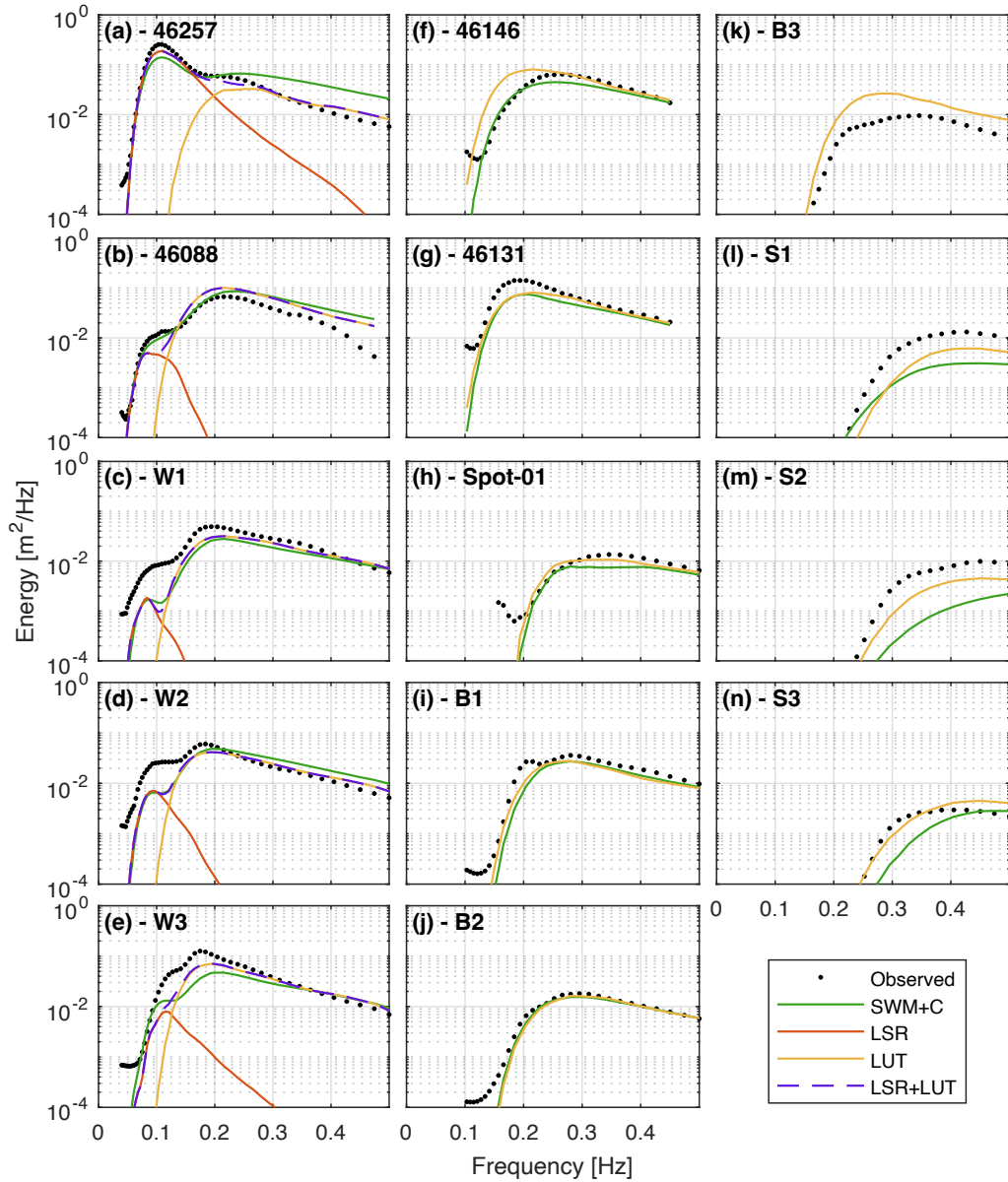


Figure 12: Mean modeled (colored lines) and observed (black dots) energy versus frequency at observations sites exposed to offshore wave energy in panels (a)-(e). Modeled and observed energy averaged over time frames where observations are available (Table 1)

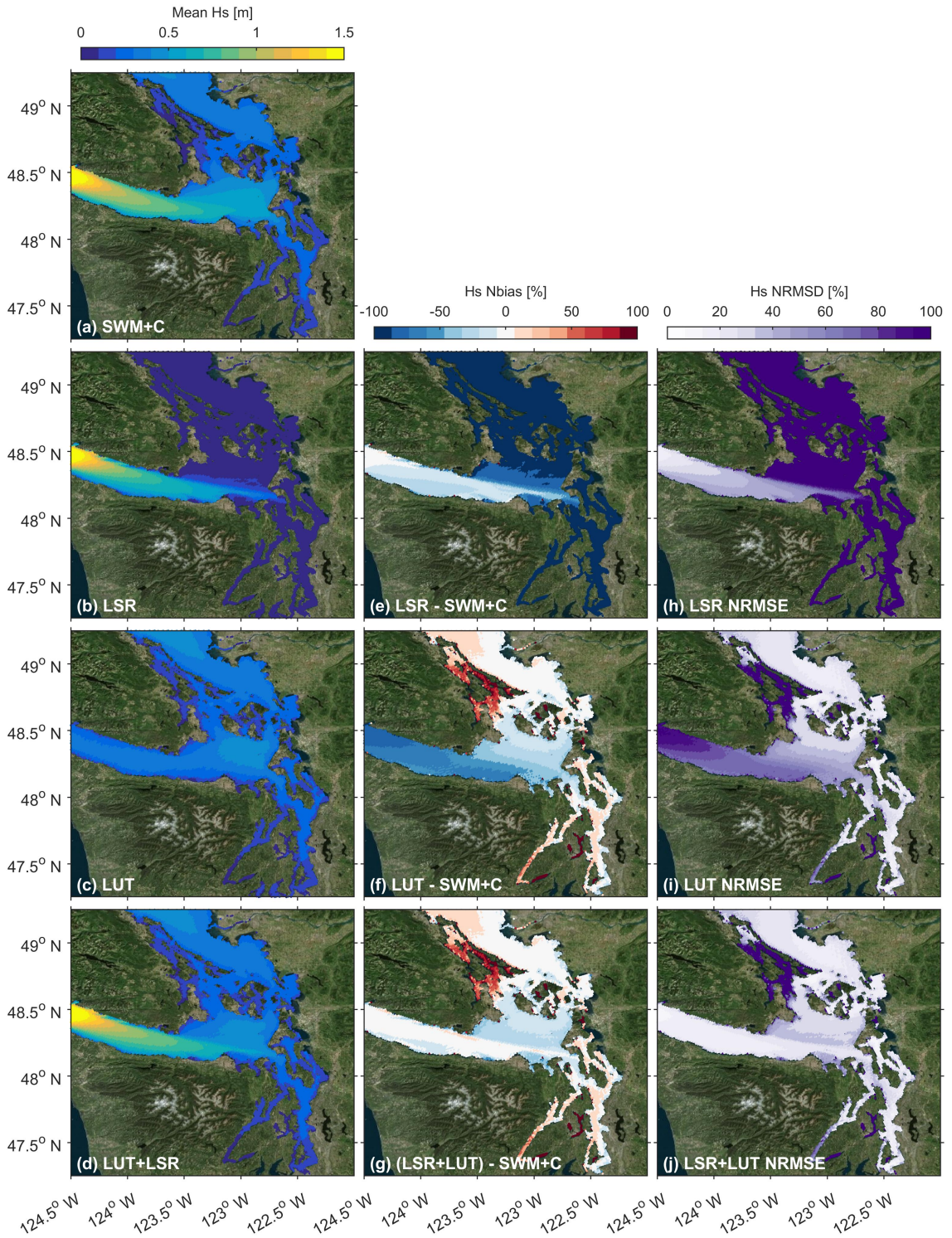


Figure 13: Mean SWM (a), LSR (b), LUT (c), and LSR+LUT (d) modeled wave heights from Oct 1 2020 through Nov 30 2020. Mean bias with SWM+C predictions for LSR (e), LUT (f), and LSR+LUT (g). Root-mean-squared-difference (RMSD) with SWM+C predictions for LSR (h), LUT (i), and LSR+LUT (j).

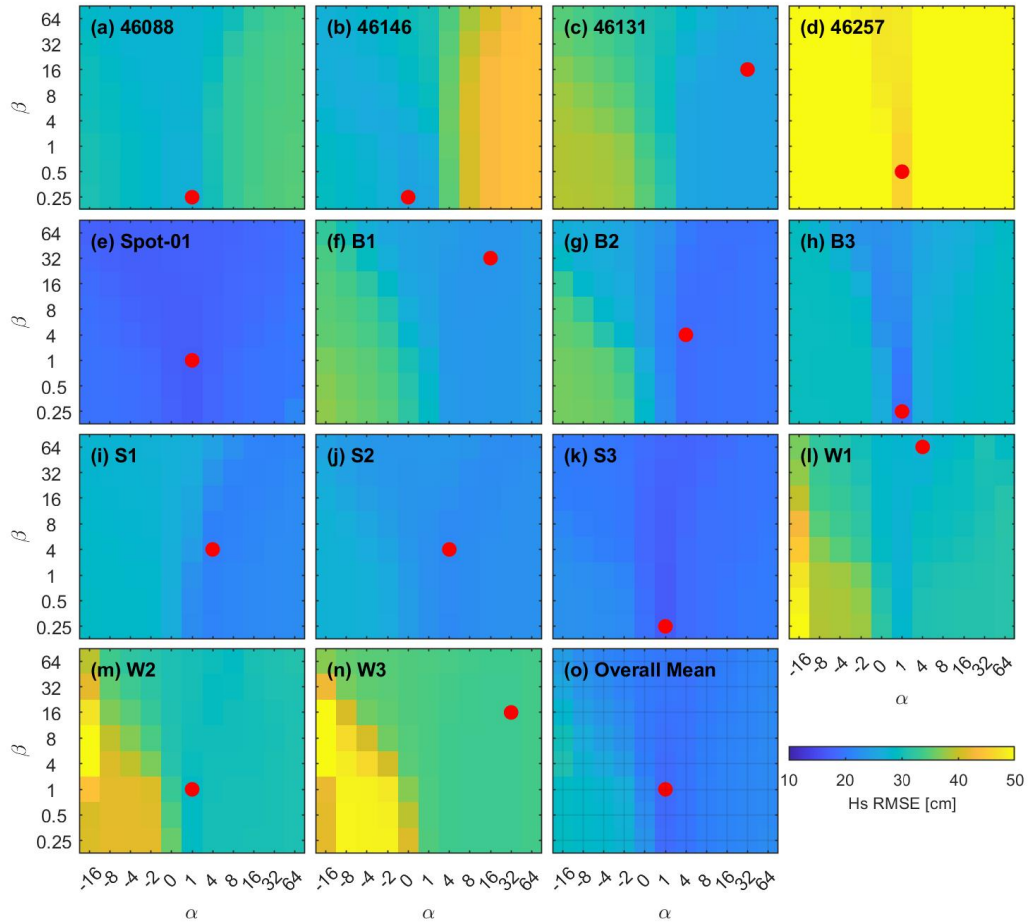


Figure A1: H_s root-mean-squared-error (RMSE) versus α and β at each observation site (Table 1) and a simple average across all locations except for 46257 due to its high exposure to remotely generated waves (n). Minimum RMSE is indicated by the filled red circle.